Inorganic Chemistry
ARTICLE
pubs.acs.org/IC

Structural, Electronic, and Magnetic Properties of Quasi-1D Quantum Magnets [Ni(HF$_2$)(pyz)$_2$]X (pyz = pyrazine; X = PF$_6^-$, SbF$_6^-$) Exhibiting Ni-FHF-Ni and Ni-pyz-Ni Spin Interactions

Jamie L. Manson,[*,†] Saul H. Lapidus,[‡] Peter W. Stephens,[*,‡] Peter K. Peterson,[†] Kimberly E. Carreiro,[†] Heather I. Southerland,[†] Tom Lancaster,[§] Stephen J. Blundell,[§] Andrew J. Steele,[§] Paul A. Goddard,[§] Francis L. Pratt,[∥] John Singleton,[⊥] Yoshimitsu Kohama,[⊥] Ross D. McDonald,[⊥] Rico E. Del Sesto,[⊗] Nickolaus A. Smith,[○] Jesper Bendix,[#] Sergei A. Zvyagin,[▽] Jinhee Kang,[◆] Changhoon Lee,[◆] Myung-Hwan Whangbo,[◆] Vivien S. Zapf,[⊥] and Alex Plonczak[⊥]

[†]Department of Chemistry and Biochemistry, Eastern Washington University, Cheney, Washington 99004, United States
[‡]Department of Physics and Astronomy, State University of New York, Stony Brook, New York 11794, United States
[§]Clarendon Laboratory, Department of Physics, Oxford University, Oxford OX1 3PU, U.K.
[∥]ISIS Pulsed-Muon Facility, Rutherford-Appleton Laboratory, Chilton, Oxfordshire OX11 0QX, U.K.
[⊥]NHMFL, [⊗]MPA, and [○]MST Divisions, Los Alamos National Laboratory, Los Alamos, New Mexico 87545, United States
[#]Department of Chemistry, University of Copenhagen, Copenhagen DK-2100, Denmark
[▽]Hochfeld-Magnetlabor Dresden (HLD), Forschungszentrum Dresden-Rossendorf (FZD), D-01314 Dresden, Germany
[◆]Department of Chemistry, North Carolina State University, Raleigh, North Carolina 27695, United States

Supporting Information

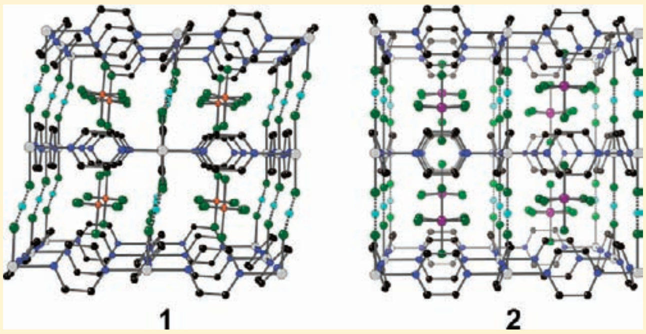

ABSTRACT: [Ni(HF$_2$)(pyz)$_2$]X {pyz = pyrazine; X = PF$_6^-$ (**1**), SbF$_6^-$ (**2**)} were structurally characterized by synchrotron X-ray powder diffraction and found to possess axially compressed NiN$_4$F$_2$ octahedra. At 298 K, **1** is monoclinic ($C2/c$) with unit cell parameters, a = 9.9481(3), b = 9.9421(3), c = 12.5953(4) Å, and β = 81.610(3)° while **2** is tetragonal ($P4/nmm$) with a = b = 9.9359(3) and c = 6.4471(2) Å and is isomorphic with the Cu-analogue. Infinite one-dimensional (1D) Ni-FHF-Ni chains propagate along the c-axis which are linked via μ-pyz bridges in the ab-plane to afford three-dimensional polymeric frameworks with PF$_6^-$ and SbF$_6^-$ counterions occupying the interior sites. A major difference between **1** and **2** is that the Ni−F−H bonds are bent (~157°) in **1** but are linear in **2**. Ligand field calculations (LFT) based on an angular overlap model (AOM), with comparison to the electronic absorption spectra, indicate greater π-donation of the HF$_2^-$ ligand in **1** owing to the bent Ni−F−H bonds. Magnetic susceptibility data for **1** and **2** exhibit broad maxima at 7.4 and 15 K, respectively, and λ-like peaks in dχT/dT at 6.2 and 12.2 K that are ascribed to transitions to long-range antiferromagnetic order (T_N). Muon-spin relaxation and specific heat studies confirm these T_N's. A comparative analysis of χ vs T to various 1D Heisenberg/Ising models suggests moderate antiferromagnetic interactions, with the primary interaction strength determined to be 3.05/3.42 K (**1**) and 5.65/6.37 K (**2**). However, high critical fields of 19 and 37.4 T obtained from low temperature pulsed-field magnetization data indicate that a single exchange constant (J_{1D}) alone is insufficient to explain the data and that residual terms in the spin Hamiltonian, which could include interchain magnetic couplings ($J_\perp$), as mediated by Ni-pyz-Ni, and single-ion anisotropy (D), must be considered. While it is difficult to draw absolute conclusions regarding the magnitude (and sign) of $J_\perp$ and D based solely on powder data, further support offered by related Ni(II)-pyz compounds and our LFT and density-functional theory (DFT) results lead us to a consistent quasi-1D magnetic description for **1** and **2**.

1. INTRODUCTION

Hydrogen bonding plays an integral role in numerous structure−property relationships including proton transfer in biological systems[1] and mediation of mixed-valency between dimerized oxo-centered triruthenium clusters.[2] The highly directional although flexible nature of hydrogen bonds is particularly advantageous for crystal engineering applications as molecular building blocks

Received: December 20, 2010
Published: May 20, 2011

dx.doi.org/10.1021/ic102532h | Inorg. Chem. 2011, 50, 5990–6009

(of varying sizes and geometries) can be positioned in nearly predictable manners.[3] Oftentimes, classical hydrogen bonds are comprised of O−H···O, O−H···N, and N−H···O types of donor/acceptor interactions whereas nonclassical types primarily involve C−H···X (where X is an electronegative atom or perhaps a π-bond). Typically, the strengths of such bonds are weak (5−20 kJ/mol) although sufficient to influence crystal packing.[4]

A smaller class of strong hydrogen bonds based on fluoride acceptors (e.g., O−H···F and F···H···F) also exists.[5−10] In the case of bifluoride (HF_2^- or FHF^-), which contains the strongest known hydrogen bonds, a wide range of bond enthalpies have been calculated (169−241 kJ/mol)[11−15] although an experimentally determined value of 163 kJ/mol has been obtained by gas-phase ion-cyclotron resonance.[16] The H···F bond strength in FHF^- rivals some of the known covalent bond energies (e.g., O−O = 145 kJ/mol, F−F = 158 kJ/mol, and N−N = 170 kJ/mol)[17] and moreover, it is substantially stronger than the intermolecular hydrogen bond found in the vapor phase of hydrofluoric acid (HF···HF = 29 kJ/mol).[3]

We are particularly interested in the self-assembly of coordination polymers using a unique combination of coordinate covalent (e.g., *M*-pyz) bonds and the aforementioned strong H···F hydrogen bonds.[6−10] Along these lines, some of us recently reported on the structural and magnetic properties of a Cu(II)-containing ($S = 1/2$) coordination polymer, $[Cu(HF_2)(pyz)_2]BF_4$, where pyz is pyrazine ($N_2C_4H_4$).[7,8] Its structure consists of six-coordinate, axially elongated CuN_4F_2 octahedra [Cu−N = 2.040(4) and Cu−F = 2.207(4) Å] which are linked in two dimensions via bridging pyz ligands to form two-dimensional (2D) square nets confined to the *ab*-plane. The bifluoride ion is also bridging and joins the layers along the *c*-axis to yield a tetragonal three-dimensional (3D) network with BF_4^- ions occupying the interstitial sites. Pyrazine ligands are counter-rotated relative to adjacent rings by 59.4(2)°, which imposes a 4-fold rotational symmetry about the Cu(II) center. Since our work emerged, two other related systems, namely, $[Cu(NO_3)(pyz)_2]PF_6$ and $[Cu(NO_2)(pyz)_2]ClO_4$, have also been described.[18,19]

$[Cu(HF_2)(pyz)_2]BF_4$ was found to be an excellent example of the $S = 1/2$ Heisenberg 2D square lattice antiferromagnet and has an intralayer Cu-pyz-Cu coupling constant (J_{2D}) of 5.7 K.[8] A σ-bonding network made up of the Cu magnetic orbitals (i.e., $d_{x^2-y^2}$ orbitals) and pyz lone-pair (p_z) orbitals leads to the observed 2D magnetism. The interlayer exchange interaction ($J_\perp$) mediated by the Cu-FHF-Cu bridges is very weak such that $[Cu(HF_2)(pyz)_2]BF_4$ undergoes a long-range magnetic order at a very low temperature (T_N = 1.54 K).[7,8] This is because the σ-orbitals of the axial HF_2^- ligand overlap with the spin-paired Cu d_{z^2} orbital.

Beyond our initial work on $[Cu(HF_2)(pyz)_2]BF_4$ we sought to substitute BF_4^- for other counterions such as octahedral PF_6^- and SbF_6^-.[9,10] Indeed, it was possible to prepare $[Cu(HF_2)(pyz)_2]PF_6$ and $[Cu(HF_2)(pyz)_2]SbF_6$, both of which crystallize in the tetragonal space group *P*4/*nmm*. The larger ionic volume of PF_6^- and SbF_6^- leads to a nearly perpendicular pyz tilt angle with respect to the 2D $[Cu(pyz)_2]^{2+}$ square layers and only slight expansion of the unit cell along the Cu-FHF-Cu direction. For reasons that are presently unclear, J_{2D} and T_N increase dramatically to 13.4 and 4.3 K, respectively, for both compounds.[9,10] For these compounds the only apparent structural difference is the pyrazine tilt angle which may be important in dictating the strength of the *M*-pyz-*M* exchange interaction.

Further to this point, it has been suggested that the π-orbitals of the pyz ring may contribute to a possible orientation dependence, but this concept remains speculative.[20] A detailed molecular orbital study, carried out by Mohri et al.[21] who utilized binuclear Cu-pyz-Cu fragments to analyze through-space and through-bond orbital contributions, showed that the dominant magnetic interaction is mediated by the superexchange between the Cu $d_{x^2-y^2}$ magnetic orbital and pyz σ lone-pair orbital which enables an antiferromagnetic coupling via a through-bond mechanism.[21] Therefore, the ligand π-orbitals appear to be inconsequential to the superexchange (a priori). Conflicting evidence is raised by employing 1,4-diazabicyclo-[2.2.2]octane (dabco) as a bridging moiety in Cu(II) coordination polymers because negligible exchange coupling is observed even though it contains only a σ-bond skeleton.[22] Granted, the coordinating N-atoms of dabco adopt a different orbital hybridization relative to pyz (sp^3 vs sp^2) and this too may be an important factor. Clearly, more electronically diverse materials are needed to better understand the origin of this behavior and those that contain two or more magnetic orbitals [e.g., Ni(II)] may prove useful in this regard.

Another important aspect of our work is to examine how efficiently the HF_2^- ligand mediates spin exchange between paramagnetic metal ions, and thus it is essential to study systems that allow the σ-orbitals of the HF_2^- ligand to overlap with an appropriate metal magnetic orbital. A promising d-metal ion for such an investigation is Ni(II) because it has two magnetic orbitals (i.e., $d_{x^2-y^2}$ and d_{z^2} orbitals) such that, if it were to form 3D solids analogous to $[Cu(HF_2)(pyz)_2]X$, both Ni-pyz-Ni and Ni-FHF-Ni spin exchange paths would be important.

Herein, we describe the synthesis and characterization of two new 3D coordination polymers, namely, $[Ni(HF_2)(pyz)_2]X$ {where X = PF_6^- (**1**) or SbF_6^- (**2**)}, which contain the desired combination of Ni-FHF-Ni and Ni-pyz-Ni moieties. In **1** and **2**, one-dimensional (1D) Ni-FHF-Ni chains are linked via pyz bridges to form 3D frameworks with PF_6^- or SbF_6^- anions occupying interstitial sites. Expectedly, the magnetic behaviors of **1** and **2** markedly differ from those of $[Cu(HF_2)(pyz)_2]X$ owing to the obvious differences in electronic structures. Long-range magnetic order occurs below Néel temperatures, T_N, of 6.2 and 12.2 K for **1** and **2**, respectively, the latter of which is the highest for any structurally characterized *M*(II)-pyz compound. The differing magnetic behaviors between **1** and **2** is attributed to the presence of bent Ni−F−H bond angles in **1** (while they are linear in **2**) for which ligand-field theory also suggests that the *D*-values for **1** and **2** are of opposite sign but similar magnitude. Density-functional theory (DFT) further shows that the spin exchange is stronger along Ni-FHF-Ni than Ni-pyz-Ni which is consistent with experimental findings.

2. EXPERIMENTAL METHODS

2.1. Syntheses. All chemicals were ACS reagent grade and used as received from commercial sources. Following a general procedure, pale blue powders of **1** and **2** were isolated in high yield (>80%) upon slow evaporation of the solvent for several days. The products were thoroughly washed with small amounts of H_2O, then Et_2O, and dried in vacuo for ~6 h. Compound **1** was prepared by mixing a 5-mL aqueous suspension of $NiCO_3$ (0.4003 g, 3.37 mmol) with 2 equiv of HPF_6 (~60% by weight in H_2O). The resulting $Ni(PF_6)_2$ solution was stirred and added to a

Table 1. Synchrotron X-ray Crystallographic Refinement Details for [Ni(HF$_2$)(pyz)$_2$]PF$_6$ (1)

T (K)	17	298
empirical formula	$C_8H_9N_4F_8PNi$	$C_8H_9N_4F_8PNi$
formula weight (g/mol)	402.85	402.85
space group	$C2/c$	$C2/c$
a (Å)	9.9322(3)	9.9481(3)
b (Å)	9.9066(3)	9.9421(3)
c (Å)	12.4803(5)	12.5953(4)
β (deg)	80.531(3)	81.610(3)
V (Å^3)	1211.26(7)	1232.4(7)
Z	4	4
ρ_{calc} (g/cm^3)	2.209	2.171
λ (Å)	0.70002(3)	0.69939(3)
R_{WP}[a]	0.06065	0.06485
R_{exp}[b]	0.04111	0.04930

[a] $R_{WP} = [\Sigma_i w_i\, (y_i^{calc} - y_i^{obs})^2/\Sigma_i w_i\, (y_i^{obs})^2]^{1/2}$, where y_i^{calc} and y_i^{obs} are the calculated and observed intensities at the i-th point in the profile, normalized to monitor intensity. The weight w_i is $1/\sigma^2$ from counting statistics, with the same normalization factor. N is the number of points in the measured profile. [b] $R_{exp} = [N/\Sigma_i w_i\, (y_i^{obs})^2]^{1/2}$.

Table 2. Synchrotron X-ray Crystallographic Refinement Details for [Ni(HF$_2$)(pyz)$_2$]SbF$_6$ (2)

T (K)	17	298
empirical formula	$C_8H_9N_4F_8SbNi$	$C_8H_9N_4F_8SbNi$
formula weight (g/mol)	493.64	493.64
space group	$P4/nmm$	$P4/nmm$
a (Å)	9.8965(3)	9.9359(3)
b (Å)	9.8965(3)	9.9359(3)
c (Å)	6.4329(2)	6.4471(2)
V (Å^3)	630.04(3)	636.47(3)
Z	2	2
ρ_{calc} (g/cm^3)	2.603	2.577
λ (Å)	0.70005(3)	0.69930(3)
R_{WP}[a]	0.0885	0.07351
R_{exp}[b]	0.04092	0.03715

[a] $R_{WP} = [\Sigma_i w_i\, (y_i^{calc} - y_i^{obs})^2/\Sigma_i w_i\, (y_i^{obs})^2]^{1/2}$, where y_i^{calc} and y_i^{obs} are the calculated and observed intensities at the i-th point in the profile, normalized to monitor intensity. The weight w_i is $1/\sigma^2$ from counting statistics, with the same normalization factor. N is the number of points in the measured profile. [b] $R_{exp} = [N/\Sigma_i w_i\, (y_i^{obs})^2]^{1/2}$.

Table 3. Selected Bond Lengths (Å) and Bond Angles (deg) for [Ni(HF$_2$)(pyz)$_2$]PF$_6$ (1)[a]

bond length or angle	T = 17 K	T = 298 K
Ni1−F5	1.984(4)	2.024(4)
Ni1−N1	2.1860(5)	2.150(4)
Ni1−N2	2.2007(4)	2.152(4)
F5···H5	1.23	1.19
P1−F1	1.641(5)	1.587(6)
P1−F2	1.747(9)	1.625(8)
P1−F4	1.600(9)	1.615(5)
C1−N1	1.366(2)	1.357(2)
C1−C2	1.399(3)	1.347(3)
Ni1−F5···H5	152	157
F5−Ni1−N1	87.6(3)	90.6(2)
F5−Ni1−N2	93.6(2)	93.3(3)
N1−Ni1−N1	180	180
N1−Ni1−N2	90.6(2)	89.4(2)
F5−Ni1−F5	180	180
F1−P1−F2	91.2(2)	89.5(2)
F1−P1−F3	83.7(2)	86.7(3)
F2−P1−F3	89.3(2)	88.7(2)
N1−C1−C2	117.4(1)	120.7(2)
C3−N2−C4	125.1(6)	118.5(3)

[a] Numbers in parentheses are the standard uncertainties computed from the least-squares (Rietveld) fits and are therefore derived purely from counting statistics; realistic experimental uncertainties are likely two to five times larger.

3-mL aqueous solution containing NH_4HF_2 (0.1923 g, 3.37 mmol) and pyrazine (0.5401 g, 6.74 mmol) to yield a green solution. For **2**, $NiF_2 \cdot 4H_2O$ (0.6010 g, 3.56 mmol) was dissolved in ∼5 mL of aqueous HF (48% by weight in H_2O) and slowly mixed with a 3-mL aqueous HF solution that contained NH_4HF_2 (0.2030 g, 3.56 mmol), pyrazine (0.5705 g, 7.11 mmol), and $NaSbF_6$ (0.9211 g, 3.56 mmol) to afford a green solution. ***Caution!*** *Hydrofluoric acid is toxic and corrosive and should be handled with great care.*

2.2. Optical Spectroscopy. Mid-IR spectra were recorded on a Thermo Avatar 360 FT-IR with a Nicolet Smart DuraSamplIR ATR accessory. Samples consisted of neat powders pressed against a single bounce diamond crystal. UV/vis/near-IR spectra were collected on a Harrick Praying Mantis diffuse reflectance apparatus mounted in a Varian Cary 5000 UV−vis spectrometer. Baseline corrected reflectance was measured for powders. Baseline involved 0 and 100% absorbance values for reference using an empty sample holder and KBr powder, respectively. Spectra were collected in reflectance mode and converted to absorbance.

2.3. Synchrotron X-ray Powder Diffraction (XRPD). Pale blue powders of **1** and **2** were individually flame-sealed in thin-walled glass capillary tubes and high-resolution powder diffraction patterns collected on the X16C beamline located at the National Synchrotron Light Source, Brookhaven National Laboratory. A Si(111) channel-cut monochromator selected a highly parallel 0.6993(2)-Å incident beam. The diffracted X-rays were analyzed by a Ge(111) single-reflection crystal and detected using a NaI scintillation counter. Measurements were made at 17 and 298 K; the capillary was rocked by a few degrees and spun at several Hz during data collection to improve particle statistics.

The TOPAS-Academic program was used to index both **1** and **2**.[23] The space groups $C2/c$ (No. 15) and $P4/nmm$ (No. 129) were hypothesized for **1** and **2**, respectively, by checking the systematic absences of Pawley whole pattern fits. The crystal structures of **1** and **2** were determined in TOPAS and Superflip,[24] respectively. The simulated annealing method implemented in TOPAS was used to determine the structure of **1**. Superflip implements charge flipping which was used to produce a density map of **2**, from which the structure was determined. After obtaining an acceptable agreement between observed and calculated XRPD patterns from the structure solution, Rietveld refinements were performed to improve the fits and carefully determine atomic positions. All heavy atoms were refined isotropically for **1** or anisotropically as in the case of **2**. Bifluoride H-atoms were fixed in position and refined isotropically for both compounds. Pyrazine H's were placed in idealized positions. Tables 1−4 contain structural parameters and refinement details as well as selected bond lengths and angles.

2.4. Temperature-Dependent Magnetization. Measurements were performed using a Quantum Design PPMS-14T magnetometer

Table 4. Selected Bond Lengths (Å) and Bond Angles (deg) for $[Ni(HF_2)(pyz)_2]SbF_6$ (2)[a]

bond length or angle	T = 17 K	T = 298 K
Ni1−F3	2.066(5)	2.099(3)
Ni1−N1	2.097(3)	2.123(2)
F3···H2	1.150	1.130
Sb1−F1	1.891(3)	1.897(2)
Sb1−F2	1.866(7)	1.890(5)
Sb1−F4	1.881(7)	1.845(5)
C1−N1	1.339(4)	1.331(3)
C1−C1A	1.402(4)	1.403(5)
Ni1−F3···H2	180	180
F3−Ni1−N1	90	90
F3−Ni1−F3A	180	180
N1−Ni1−N1	180	180
F1−Sb−F2	89.1(1)	88.9(1)
F1−Sb−F4	90.9(1)	91.2(1)
F2−Sb−F4	180	180
N1−C1−C1A	121.6(3)	121.1(2)
C1−N1−C1A	116.8(3)	117.8(2)

[a] Numbers in parentheses are the standard uncertainties computed from the least-squares (Rietveld) fits and are therefore derived purely from counting statistics; realistic experimental uncertainties are likely two to five times larger.

equipped with the VSM option. Polycrystalline samples of **1** and **2** were loaded into gelatin capsules, mounted in a plastic drinking straw, and affixed to the end of a carbon fiber rod. All of the samples were cooled in zero-field to a base temperature of 2 K and data collected on warming in a 0.1 T magnetic field. Field-dependent $M(T)$ studies were performed in an analogous fashion by first zero-field cooling to 2 K, charging the magnet to 5, 7.5, 10, or 13 T, and data taken on warming. All magnetic data were corrected for core diamagnetism using Pascal's constants and a small temperature-independent paramagnetism was taken into account as expected for Ni(II) ion.

2.5. Pulsed-Field Magnetization. The pulsed-field magnetization experiments (up to 60 T) used a 1.5 mm bore, 1.5 mm long, 1500-turn compensated-coil susceptometer, constructed from 50 gauge high-purity copper wire. When a sample is within the coil, the signal voltage V is proportional to (dM/dt), where t is the time. Numerical integration of V is used to evaluate M. The sample is mounted within a 1.3 mm diameter ampule that can be moved in and out of the coil. Accurate values of M are obtained by subtracting empty coil data from that measured under identical conditions with the sample present. The susceptometer was placed inside a ^{3}He cryostat providing temperatures down to 0.5 K. The field B was measured by integrating the voltage induced in a ten-turn coil calibrated by observing the de Haas−van Alphen oscillations of the belly orbits of the copper coils of the susceptometer.

2.6. Muon-Spin Relaxation (μSR). Zero-field muon-spin relaxation (ZF-μ^+SR) measurements on powder samples of **1** and **2** were carried out using the GPS spectrometer at the Swiss Muon Source (SμS), Paul Scherrer Institut, Villigen, CH. For these experiments, the samples were packed in Ag foil (25 μm) and mounted on a Ag backing plate.

μ^+SR involves injection of spin-polarized positive muons into a sample.[25] The positive muons stop in the material, usually in sites with high electron density, and their polarized magnetic moments precess around the local magnetic field with a frequency, $\nu = \gamma_\mu B/2\pi$, where the muon gyromagnetic ratio, $\gamma_\mu/2\pi$ is 135.5 MHz/T. Muons are unstable particles with a mean lifetime of 2.2 μs, and decay into a positron and two neutrinos, the former being preferentially emitted along the direction of muon spin. Detectors record the direction of positron emission, whose time dependence tracks the ensemble of muon spins rotating around their respective local B-fields.

In these experiments, the detectors are divided into a forward (F) and backward (B) detector bank, and the direction of preferential positron emission is represented by the asymmetry between $N_F(t)$ and $N_B(t)$, the number of positrons detected in each detector bank as a function of time. The decay positron asymmetry function, $A(t)$, which is proportional to the spin polarization of the muon ensemble, is defined in (eq 1) where α is an experimentally determined instrumental calibration constant.[25]

$$A(t) = \frac{N_F(t) - \alpha N_B(t)}{N_F(t) + \alpha N_B(t)} \qquad (1)$$

2.7. Specific Heat (C_p). Measurements were made on $[Ni(HF_2)(pyz)_2]SbF_6$ (**2**) using traditional heat-pulse[26] and dual-slope thermal relaxation methods.[27] The advantage of the dual-slope method is that C_p data can be collected quickly and precisely, which is important to determine the transition temperature (T_N) at several magnetic fields. However, this method usually requires excellent thermal contact between sample and thermometer, that is, it can only be used in cases of minimal tau-2 effects.

These measurements were performed on a 1.700 mg powder sample mixed with a small amount of Apiezon-N grease and pressed between copper foils which acted as a mechanical/thermal support. The sample probe was mounted in an Oxford 15 T superconducting magnet system capable of reaching a base temperature of 0.5 K. The addenda specific heat due to Apiezon-N, copper foil, and sample holder platform was measured separately and amounted to ∼60% of the total specific heat over the entire temperature range (4 and 16 K). After subtracting the addenda contribution from the total specific heat, the specific heat of the sample was obtained. Excellent agreement (within 10%) between the two methods confirmed that tau-2 effects could be neglected.

2.8. High-Field Electron-Spin Resonance (ESR). Measurements in the frequency range 53−425 GHz were performed at temperatures down to 1.6 K using a tunable-frequency home-built ESR spectrometer (similar to that described in ref 28) equipped with a high-homogeneity 16 T superconducting magnet and VDI diodes as tunable sources of millimeter-wave radiation (product of Virginia Diodes Inc.).

2.9. DFT Calculations. Using 298 K structural data, we evaluated possible spin exchange parameters of $[Ni(HF_2)(pyz)_2]PF_6$ (**1**) and $[Ni(HF_2)(pyz)_2]SbF_6$ (**2**) by performing a mapping analysis based on spin-polarized DFT calculations. Our calculations employed a projector augmented wave method implemented in the Vienna *ab initio* simulation package[29] with the generalized gradient approximation (GGA)[30] for the exchange-correlation functional, the plane-wave cutoff energy of 400 eV, a set of 8 k-points for the irreducible Brillouin zone, and a threshold of 10^{-6} eV for energy convergence. To include the effect of electron correlation associated with Ni 3d states, we carried out GGA plus on-site repulsion U (GGA+U) calculations with the effective U = 4 eV on the Ni atoms.[31]

2.10. Ligand Field Calculations (LFT). Calculations were performed using the program package LIGFIELD.[32] All calculations employed the complete $3d^8$ configuration. Parameter fits were performed by iterative rediagonalizations of the full matrices. The χ^2 minimizations were done by use of a Leuwenberg-Marquardt algorithm using equal weights for all observations. The quoted uncertainties on parameters are scaled values ensuring the model to pass statistics. They are in most cases upper bounds on the actual uncertainties which would be obtained by a rigorous treatment including errors on the observations.

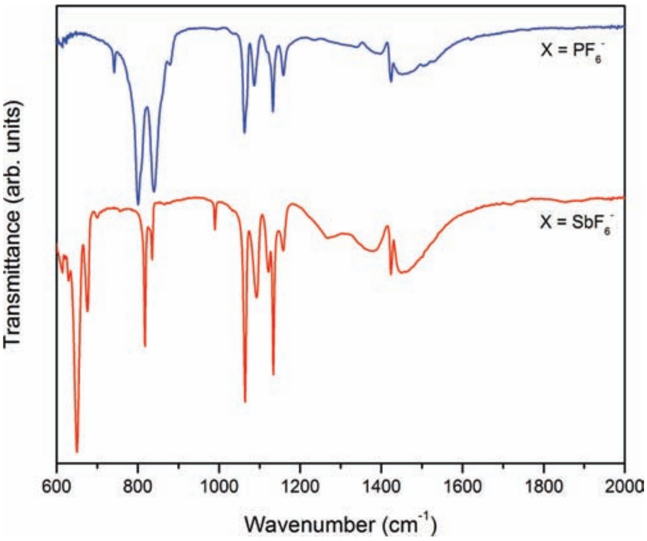

Figure 1. Mid-IR spectra of neat polycrystalline $[Ni(HF_2)(pyz)_2]X$ recorded at 298 K.

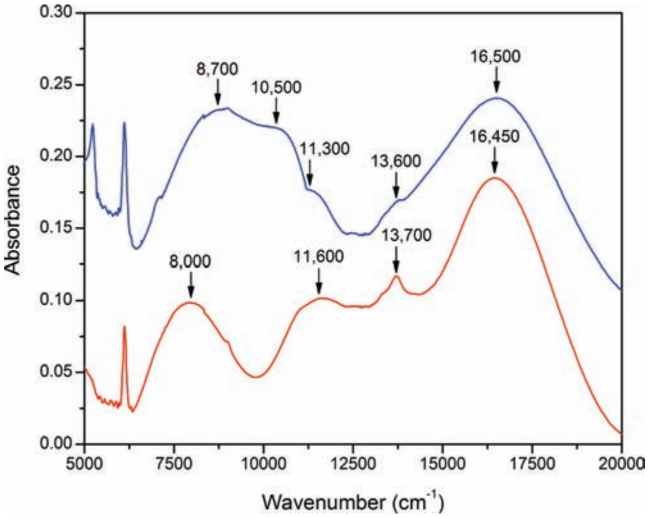

Figure 2. Diffuse reflectance electronic absorption spectra for polycrystalline $[Ni(HF_2)(pyz)_2]PF_6$ (**1**) (blue) and $[Ni(HF_2)(pyz)_2]SbF_6$ (**2**) (red) obtained at 298 K.

3. RESULTS

3.1. Vibrational Spectroscopy. The room temperature infrared spectra of **1** and **2** measured between 600 and 4000 cm^{-1} are very similar to those of their Cu(II) counterparts and confirm the presence of the HF_2^- and pyz molecular components (Figure 1).[10] Common features of both spectra are the somewhat broad H−F bending and asymmetric stretching modes that occur between 1200 and 1600 cm^{-1}.[5] Pyrazine ring C═C/C═N stretching and in-plane C═C/C═N bending modes lie between 1000 and 1200 cm^{-1}.[33] In addition, sharp, medium intensity peaks between 800 and 840 cm^{-1} are assigned to pyz C−H out-of-plane deformation modes. Nonmetal P−F/Sb-F stretching and F−P−F/F−Sb−F out-of-plane deformation modes appear as two strong peaks (800−900 cm^{-1} for PF_6^-; 600−700 cm^{-1} for SbF_6^-).[34] The symmetric and asymmetric C−H stretching modes of the pyz ligands appear as two very weak features between 3100 and 3160 cm^{-1}.

3.2. Ligand-Field Spectra and Analysis. Unpolarized diffuse reflectance spectra for **1** and **2** were obtained at 298 K between 250 and 2000 nm (5,000−40,000 cm^{-1}) and are shown together in Figure 2, highlighting the spectral region between 5,000 and 20,000 cm^{-1}. For an S = 1 Ni(II) ion (3d^8) in an octahedral crystal field three spin-allowed transitions are potentially observable: $^3T_1(F) \leftarrow {}^3A_2$, $^3T_1(F) \leftarrow {}^3A_2$, and $^3T_1(P) \leftarrow {}^3A_2$. Any distortion of the chromophore, such as the lowered symmetry in the *trans*-N_4F_2 ligand surroundings of **1** and **2** will create peak broadening or splitting in the electronic absorption spectrum. The magnitude of these splittings is determined mainly by differences in ligand field parameters of the ligators. For instance, the combination of nitrogen and fluoride ligators is well-known to produce significant splittings of the corresponding spin-allowed transitions in tetragonal chromium(III) complexes.[35]

To simplify the labeling of the spectral assignments for **1**,[36] we approximated the symmetry of the NiN_4F_2 chromophore as D_{4h}, despite its true monoclinic symmetry. For **1** and **2**, sharp peaks in the near-IR could be vibrational or electronic in origin. However, if electronic, their small width would require them to be spin-forbidden transitions, of which the lowest occur for high-spin 3d^8 at $8B + 2C \approx 16B$ in the cubic strong field limit. With positions around 6000 cm^{-1} this would imply values for the Racah B parameter below 400 cm^{-1}. For Ni(II) in weakly nephelauxetic ligand surroundings, this is unreasonable, and these bands must be vibrational overtones or combination bands. Compound **1** shows two well resolved absorptions centered at 8,700 and 10,500 cm^{-1} as deduced by Gaussian fits; these peaks are assigned as split components of the $^3E_g(D_{4h}) \leftarrow {}^3B_{1g}(D_{4h})$ transition, which has an average energy of 9,600 cm^{-1}. A shoulder near 11,300 cm^{-1} is attributed to $^3B_{2g}(D_{4h}) \leftarrow {}^3B_{1g}(D_{4h})$, which is the last component of the $^3T_2(F)$ state of cubic parentage. These assignments (I) are in line with the conventional ordering of the spectrochemical series. However, the significant geometric compression of the Ni-coordination sphere in **1**, along with DFT calculations, suggest an alternative assignment (II) for these bands: $^3B_{2g}(D_{4h}) \leftarrow {}^3B_{1g}(D_{4h})$ followed by rhombic split components of $^3E_g(D_{4h}) \leftarrow {}^3B_{1g}(D_{4h})$. The average energy of all three transitions, 10,200 cm^{-1}, corresponds to the cubic ligand field parameter; $\Delta \equiv 10Dq$ and thus Dq = 1020 cm^{-1}. The weak feature at 13,600 cm^{-1} is likely due to a combination of spin-forbidden $^1B_{1g}(D_{4h}) \leftarrow {}^3B_{1g}(D_{4h})$ and $^1A_{1g}(D_{4h}) \leftarrow {}^3B_{1g}(D_{4h})$ bands. A broad peak at 16,500 cm^{-1} is assigned to overlapping, spin-allowed $^3E_g(D_{4h}) \leftarrow {}^3B_{1g}(D_{4h})$ and $^3A_{2g}\{D_{4h},F(R_3)\} \leftarrow {}^3B_{1g}(D_{4h})$ transitions.

The tetragonal (D_{4h}) symmetry of **2** leads to fewer features in its spectrum. Lowest is a slightly asymmetric peak at 8,000 cm^{-1} assigned to the $^3E_g(D_{4h}) \leftarrow {}^3B_{1g}(D_{4h})$ excitation. The other split component of $^3T_2(O_h)$, namely, $^3B_{2g}(D_{4h})$ follows at 11,600 cm^{-1}. The cubic ligand field parameter has the value of the weighted average $\{2E[{}^3E_g(D_{4h})] + E[{}^3B_{2g}(D_{4h})]\}/3$ = 9,200 cm^{-1} = $\Delta \equiv 10Dq$; thus Dq = 920 cm^{-1}). Despite their similar NiN_4F_2 cores, Δ differs by about 10% for **1** and **2**. For a parameter with a radial variation proportional to r^{-5} this difference can be rationalized by the observed bond length differences between the two 298 K structures (cf. sect. 3.3). Weak and strong absorptions at 13,700 and 16,450 cm^{-1}, correspond to $\{{}^3B_{2g}(D_{4h}) \leftarrow {}^3B_{1g}, {}^1A_{1g}(D_{4h}) \leftarrow {}^3B_{1g}(D_{4h})\}$ and $^3E_g(D_{4h}) \leftarrow {}^3B_{1g}(D_{4h})$ (along with overlapping $^3A_{2g}\{D_{4h}, F(R_3)) \leftarrow {}^3B_{1g}(D_{4h})\}$ transitions, respectively. Intense absorptions for **1** and **2** also occur above 28,000 cm^{-1} that we ascribe to the $^3A_{2g}(D_{4h})$, $^3E_{1g}\{D_{4h}, P(R_3)\} \leftarrow {}^3B_{1g}(D_{4h})$ transition.

The peak assignments for **1** and **2** were made by comparison to $Ni(NH_3)_4(NCS)_2$,[37] $Ni(py)_4X_2$ (py = pyridine; X = Cl^-, Br^-)[38a,b] $Ni(pyz)_2X_2$,[38c] $Ni(pyz)X_2$,[38c] the analogous pyrazole-based[39] complexes, and $Ni(vinim)_4(SiF_6)_2$ (vinim = vinylimidazole)[40] as they possess similar ligand fields. For $Ni(py)_4X_2$, Dq = 900 and 845 cm^{-1}, and $Ni(pyz)X_2$, Dq = 877 and 870 cm^{-1}, which emphasizes the stronger crystal field of Cl^- relative to Br^-.[39c] The 2D $Ni(pyz)_2X_2$ square lattices exhibit higher Dq values of 1,050 and 1,040 cm^{-1} for X = Cl^- and Br^-, respectively, as imposed by four bound pyz ligands. A Dq value of 740 cm^{-1} and a spin−orbit coupling constant of 668 cm^{-1} have been reported for $KNiF_3$.[41] Being that Dq for **1** and **2** is larger than those of $Ni(pyz)_2X_2$, the axially coordinated F's clearly influence their electronic structures and, with regard to the spectrochemical series, it follows that $Br^- < Cl^- < HF_2^- <$ py ∼ pyz.

An Angular Overlap Model (AOM)[42] analysis of the observed transition energies was performed to obtain a detailed ligand field description of the bonding in **1** and **2**. To gain confidence in the assignments and avoid initial overparametrization, the analysis was carried out in a hierarchical, stepwise fashion. Initially, the systems were treated as cubically averaged, both in terms of geometries and by pertinent averaging of the observed transitions. Using a σ-only model, this resulted in the following optimized parameters (with the constraint that $C = 4.25B$ for all cases):[43]

For **1**; $e_\sigma^{Average} = 3414(10)$ cm^{-1}, $B = 849(3)$ cm^{-1} (band position deviations from 5 to 40 cm^{-1}).

For **2**; $e_\sigma^{Average} = 3287(160)$ cm^{-1}, $B = 861(52)$ cm^{-1} (band position deviations from 77 to 661 cm^{-1}).

As discussed above, the difference in $e_\sigma^{Average}$ for the two compounds is less than 10% and is primarily related to the shorter Ni−F bonds in **1**. Relaxing the model to encompass different σ-values for fluoride and nitrogen ligators and considering the spectral data for the tetragonal split components, produces the following optimized parameters:

For **1**, assignment I; $e_\sigma^F = 2670(161)$ cm^{-1}, $e_\sigma^N = 3720(68)$ cm^{-1}; $B = 847(16)$ cm^{-1} (band position deviations from 25 to 173 cm^{-1}).

For **1**, assignment II; $e_\sigma^F = 4627(65)$ cm^{-1}, $e_\sigma^N = 2901(25)$ cm^{-1}; $B = 848(5)$ cm^{-1} (band position deviations from 4 to 59 cm^{-1}).

For **2**; $e_\sigma^F = 1701(110)$ cm^{-1}, $e_\sigma^N = 3903$ (48) cm^{-1}; $B = 857(12)$ cm^{-1} (band position deviations from 11 to 124 cm^{-1}).

In this parametrization, the difference in e_σ^F values between **1** and **2** is too large to be explained by the structural differences and reflects that the system of nonlinear equations for **1** is poorly characterized by four observations and three free parameters assuming that π-interactions are neglected. From the four observations with tetragonal parentage it is possible to determine four parameters by including an isotropic π-parameter for *either* fluoride or pyrazine. However, only some of the six possible combinations of π-parameters and spectral data yield physically reasonable values for these parameters. Thus, the following values were fitted: e_π^F (**1**, assignment I) = 433 cm^{-1}; e_π^N = 770 cm^{-1} (**1**, assignment II) and e_π^N = 307 cm^{-1} (for **2**). It should be noted that with zero degrees of freedom, there are no deviations from the observations and likewise no uncertainties on the fitted parameter values.

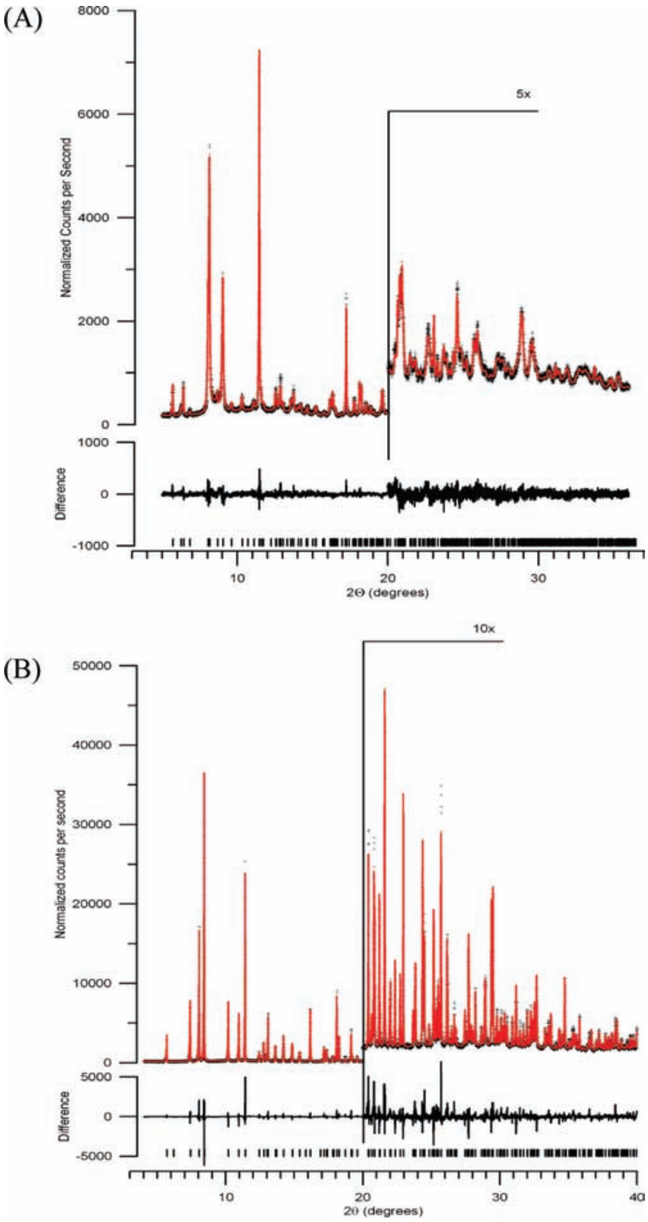

Figure 3. Synchrotron X-ray powder diffraction data obtained at 298 K for: (A) $[Ni(HF_2)(pyz)_2]PF_6$ (**1**) and (B) $[Ni(HF_2)(pyz)_2]SbF_6$ (**2**). Black symbols and red lines represent the experimental data and Rietveld fit, respectively. The solid black line at the bottom of each graph is the difference between the observed and calculated patterns.

Finally, using the experimental ligator coordinates for **1** and the (rhombic) split components assigned to its electronic spectrum, the following parameters were found:

Assignment I ($e_\sigma^N = 3720$ cm^{-1} fixed): $e_\sigma^F = 3128(166)$ cm^{-1}, $e_\pi^{F\parallel} = 947(182)$ cm^{-1}, $e_\pi^{N\perp} = -244(179)$ cm^{-1}, $B = 851(13)$ cm^{-1} (band position deviations from 23 to 143 cm^{-1}).

Assignment II ($B = 847$ cm^{-1} fixed): $e_\sigma^F = 4173(2)$ cm^{-1}, $e_\pi^{F\parallel} = 1080(3)$ cm^{-1}, $e_\sigma^N = 4299(4)$ cm^{-1}, $e_\pi^{N\perp} = 1400(4)$ cm^{-1} (band position deviations from 0 to 2 cm^{-1}).

As gleaned by a gross reduction in statistical errors, assignment II better reproduces the spectroscopic data of **1** and is therefore the most appropriate model based on 298 K data.

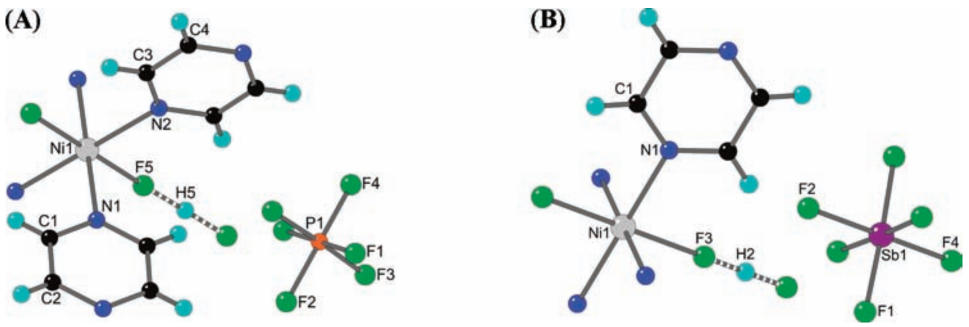

Figure 4. Room temperature asymmetric units and atom labeling schemes for (A) $[Ni(HF_2)(pyz)_2]PF_6$ (**1**) and (B) $[Ni(HF_2)(pyz)_2]SbF_6$ (**2**). Dashed cylinders represent hydrogen bonds.

Importantly, it was not possible to obtain reasonable fits of the positions of the rhombic split components of the first spin-allowed band in the spectrum of **1** with either of the alternative assignments without allowing for anisotropic π-parameters of the bifluoride ligands. Not unexpectedly, the misaligned interaction between the nonlinearly ligating HF_2^- ligand and the Ni(II) ions introduces a significant anisotropic π-parameter with a large positive value[44] in the plane of Ni-FHF. Other possibilities attempted for parametrizing the bands in the spectrum of **1** included tries with only anisotropic π-parameters for pyrazine and the inclusion of spin−orbit coupling. The latter was considered with values up to 80% of the free ion value (ζ_{3d} = 668 cm^{-1}),[35] however, rediagonalization[45] of the spin−orbit coupling matrix with respect to the ligand field parameters describing the intermediate field of **1** directly showed the sensitivity of the first spin-allowed band for spin−orbit coupling splittings to be modest ($\approx$1). Thus, the maximal effects achievable by inclusion of this parameter are on the order of the one-electron spin−orbit coupling constant.

Thus, the electronic spectra of **1** and **2** are satisfactorily parametrized with moderate nephelauxetism, nitrogen ligand-field parameters in line with those established for analogous systems,[38−40] and significant π-donor interactions with the bifluoride ligands of **1**, encompassing anisotropic contributions from the misaligned F σ-orbital.

3.3. Crystal Structures. The structures of **1** and **2** were initially determined at 298 K by *ab initio* structure solution of synchrotron powder X-ray diffraction data (Figure 3). Subsequent data sets were collected at 17 K to rule out any possible structural phase transitions although none were observed. Over this broad temperature range, both lattices contract slightly upon cooling as expected; however, the Ni−F and Ni−N bond lengths change fairly dramatically but not in the same way. In the following, we will describe only the 298 K structures of **1** and **2** in detail but make note of these bond length variations in sect. 5.1.

*3.3.1. [Ni(HF₂)(pyz)₂]PF₆ (**1**).* The atom labeling scheme is shown in Figure 4a. $[Ni(HF_2)(pyz)_2]PF_6$ (**1**) has monoclinic (*C*2/*c*) symmetry at 298 K in contrast to the Cu-analogue which is tetragonal (*P*4/*nmm*).[9] The Ni(II) ion resides on an inversion center whereas P1, F2, F4, and H5 occupy 2-fold rotation axes; all other atoms occupy general positions. One crystallographically unique Ni(II) site exists which is coordinated to four different N-donors from pyrazine ligands at an average distance of 2.15 Å. The observed tetragonally compressed octahedron is completed by *trans*-coordination of two F5 atoms (from HF_2^-) along the axial positions with Ni1−F5 bond lengths of 2.02 Å. The difference between the axial and equatorial bond lengths is 7% which is much larger than that found in **2**. Symmetry about the Ni(II) center requires that *trans*−N1−Ni1−N1A, N2−Ni1−N2A, and F5−Ni1−F5A bond angles be rigorously 180°, and despite this, the NiN_4F_2 coordination sphere displays a slight rhombic distortion as supported by the *cis* bond angles N1−Ni1−N2, N1−Ni1−F5, and N2−Ni1−F5 which are 90.6, 89.4, and 93.3°, respectively.

Each Ni(II) center is linked through four bridging pyz ligands in the *ab*-plane to afford nominal 2D square layers as shown in Figure 5a. Although the *a*- and *b*-axis dimensions only slightly differ, the Ni-pyz-Ni separations are identical (within experimental error) at 7.03 Å. The pyz ligands form slightly nonlinear bridges between Ni(II) centers such that the N-donor atoms of the pyz ring lie just off of the Ni···Ni trajectory. From Figure 5a it is recognized that two unique pyz tilt angles exist where one of the rings is rotated 88.5° away from the *ab*-plane while the other pyz exhibits a reduced tilt angle of 53.1° relative to the same plane. Each layer is slightly offset with respect to adjacent layers and are joined together along the *c*-axis by HF_2^- pillars to yield a 3D coordination polymer (Figure 6a) with Ni-FHF-Ni separations of 6.30 Å which is ~2.4% shorter than the corresponding distance in **2**. Despite the staggered layer packing, all NiN_4F_2 octahedra share the same spatial orientation and are non-tilted.

The HF_2^- molecule in **1** is linear and symmetric with H5···F5 bond lengths of 1.19 Å which yields an F···F distance of 2.38 Å. Unlike **2** where linear Ni−F···H bonds occur; these bonds in **1** are significantly bent at an angle of ~157°. The coordinative nature of the HF_2^- ligand is far more flexible than that encountered in azide (N_3^-), for example, because of the inherently different electronic structure (and lack of π-bonds in HF_2^-) that each possesses. Bifluoride apparently offers greater directionality owing to its internal hydrogen bonds as opposed to the stronger covalent bonds in N_3^-.

The PF_6^- ions required for charge compensation occupy all of the framework interiors as illustrated in Figure 6a. Along two of the three unique directions, the PF_6^- molecules are aligned uniformly and share the same orientation; however, they alternately stagger along the *c*-axis which contrasts the arrangement found in **2**. The octahedral PF_6^- ion is somewhat distorted and contains four different P−F bond lengths that range between 1.56 and 1.63 Å [average = 1.60 Å]. The F−P−F bond angles are also distorted.

*3.3.2. [Ni(HF₂)(pyz)₂]SbF₆ (**2**).* Figure 4b provides the atom labeling scheme for **2**. Compound **2** is isomorphic with $[Cu(HF_2)(pyz)_2]SbF_6$ and the Ni and H2 atoms occupy $\bar{4}2m$ symmetry sites while Sb1, F2, and F4 have 4*mm* point symmetry.[10]

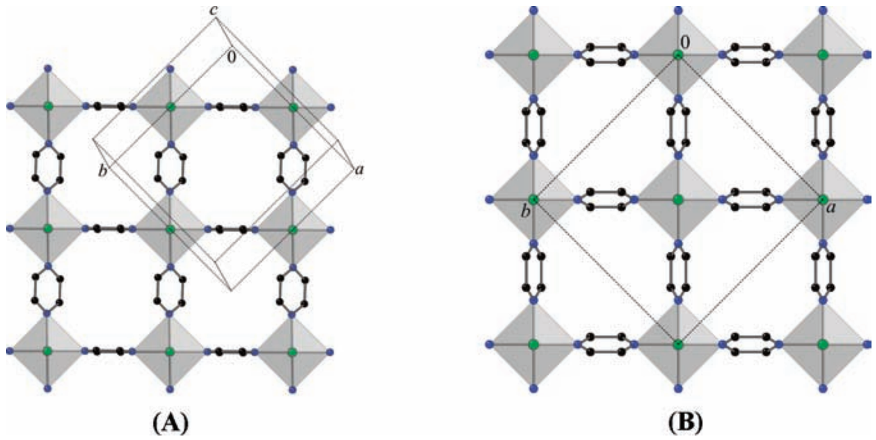

Figure 5. Comparison of the 2D $[Ni(pyz)_2]^{2+}$ square lattices observed in (A) $[Ni(HF_2)(pyz)_2]PF_6$ (**1**) and (B) $[Ni(HF_2)(pyz)_2]SbF_6$ (**2**) viewed normal to the layer direction. The illustrations correspond to the 298 K crystal structures and the unit cells are indicated by the dashed lines. Note the relative orientations of the pyz rings; *trans*-pyz ligands have the same orientation in **1** but are counter-rotated in **2** (due to the 4-fold rotational symmetry of the Ni ion in the latter). ZF_6^- (Z = P or Sb) counterions and pyz H-atoms have been omitted for clarity.

The Ni coordination sphere consists of compressed NiN_4F_2 octahedra composed of four N-donors (from pyz) in the equatorial plane [Ni1−N1 = 2.12 Å] and two axial F3-donors (from HF_2^-) at slightly shorter distances of 2.10 Å. The difference between the Ni−F and Ni−N bond lengths is a mere 1.1% and reflects a weak distortion of the NiN_4F_2 chromophore as compared to a 14.1% difference between Cu−F and Cu−N bonds in $[Cu(HF_2)(pyz)_2]SbF_6$.[10] A similarly weak tetragonal compression of 1.5% has been reported for 2D layered K_2NiF_4.[46] Interestingly, the NiN_4F_2 octahedron in **2** is axially compressed whereas a strong elongation occurs in the Cu-analogue.

The extended structure of **2** is that of a 3D coordination polymer where NiN_4F_2 octahedra are linked in two dimensions via bridging pyz ligands to form 2D $[Ni(pyz)_2]^{2+}$ square layers in the *ab*-plane (Figure 5b). Bifluoride ligands join the layers together along the *c*-axis to form a rigid pseudocubic network as shown in Figure 6b. The Ni-pyz-Ni and Ni-FHF-Ni distances are 7.03 and 6.45 Å, respectively. Pyrazine rings tilt out of the *ab*-plane by 72.8° which is ~8.6° (~11.8%) less than the near-vertical disposition observed in $[Cu(HF_2)(pyz)_2]SbF_6$ (81.4°).[10] The longer Cu−F bond distance (as compared to Ni−F in **2**) invariably allows the greater tilt angle.

Differential electron density maps indicate a symmetric placement of H2 about the midpoint between F3 and F3A in the HF_2^- ligand. In the final stages of refinement, the H2-atom position was fixed, giving equivalent H···F bond lengths of 1.13 Å, an F···F distance of 2.26 Å, and a linear F3···H2···F3A bond angle. These geometric parameters are nearly identical to those reported for $[Cu(HF_2)(pyz)_2]SbF_6$.[10]

The SbF_6^- counterions in **2** occupy the nominal body-centered positions within the framework with the Sb-centered octahedra being offset from the ideal position by 0.62 Å along the *c*-axis (see Figure 6b). Pseudochains of SbF_6^- ions form uniform stacks throughout the *c*-channels but are staggered in the opposite sense relative to adjacent (parallel) channels. Additionally, the pyz rings are tilted in a manner that produces weak nonclassical F···H−C hydrogen bonds with F···H distances of 2.54 Å. The SbF_6^- counterion has a reduced symmetry relative to the NiN_4F_2 chromophore although the Sb−F bond lengths are similar [Sb−F1 = 1.90, Sb−F2 = 1.89, and Sb−F4 = 1.85 Å]. Despite this similarity in Sb−F bond lengths, the molecule is slightly distorted from ideal O_h symmetry as evidenced by the F1−Sb−F2, F1−Sb−F4, and F1−Sb−F1 bond angles of, respectively, 88.9, 91.2, and 177.7°. The observed distortion, however, is not atypical of this anion.

The nominally square 2D $[Ni(pyz)_2]^{2+}$ layers found in **1** and **2** exhibit nearly identical geometrical parameters to those of $NiX_2(pyz)_2$ where X is Br^-, NCO^-, and NCS^-.[47−49] Axial sites are occupied by X^- whereas $Ni-N_{pyz}$ bonds take up the equatorial sites. Compressed NiN_6 octahedra with Ni−N distances of 2.14 Å (X = NCO^-)[48] and 2.16 (X = NCS^-)[49] are observed while an elongated stereochemistry was found for X = Br^- [Ni−N = 2.15 Å] due to the bulky anion.[47] The in-plane Ni···Ni distances vary only slightly among these compounds and range between 7.06 and 7.12 Å, also consistent with **1** and **2**. In these 2D systems, the layers pack in a staggered motif owing to the protruding X^-. The Ni ions in one layer lie vertically above and below the midpoints of the squares formed by Ni atoms in adjacent layers.

3.4. Magnetic Susceptibility of $[Ni(HF_2)(pyz)_2]PF_6$ (1).

A conventional magnetometer measures the magnetization (M) of a material and thus the magnetic susceptibility is extracted using the expression, $\chi = M/B$. Figure 7a shows the temperature evolution of χ for **1** as measured in a 0.1 T magnetic field. Upon cooling toward base temperature, χ reaches a maximum value of 0.0475 emu/mol at T_{max} = 7.4 K. Below T_{max}, χ decreases rapidly and plateaus near 2 K reaching a minimum value of 0.0367 emu/mol. The shape of the susceptibility curve in the region of T_{max} is typical of a low-dimensional Heisenberg antiferromagnet but not one that experiences a Haldane gap.[50]

The apparent antiferromagnetism is further substantiated by plots of χT vs T and $1/\chi$ vs T (Supporting Information, Figure S1). At 298 K, χT has a value of 0.954 emuK/mol and remains largely unchanged upon cooling down to ~100 K where it begins to decrease much more rapidly, reaching a minimum value of 0.075 emuK/mol at 2 K. This behavior is indicative of predominant antiferromagnetic correlations between S = 1 Ni(II) ions and/or some degree of zero-field splitting (ZFS) as expected for a distorted Ni(II) octahedron. From a Curie−Weiss fit of $1/\chi$ vs T over the range of 50−298 K, the Landé g-factor and Weiss constant (θ) were determined to be 2.043(1) and −12.5(1) K, respectively, which corroborates the potential coexistence of

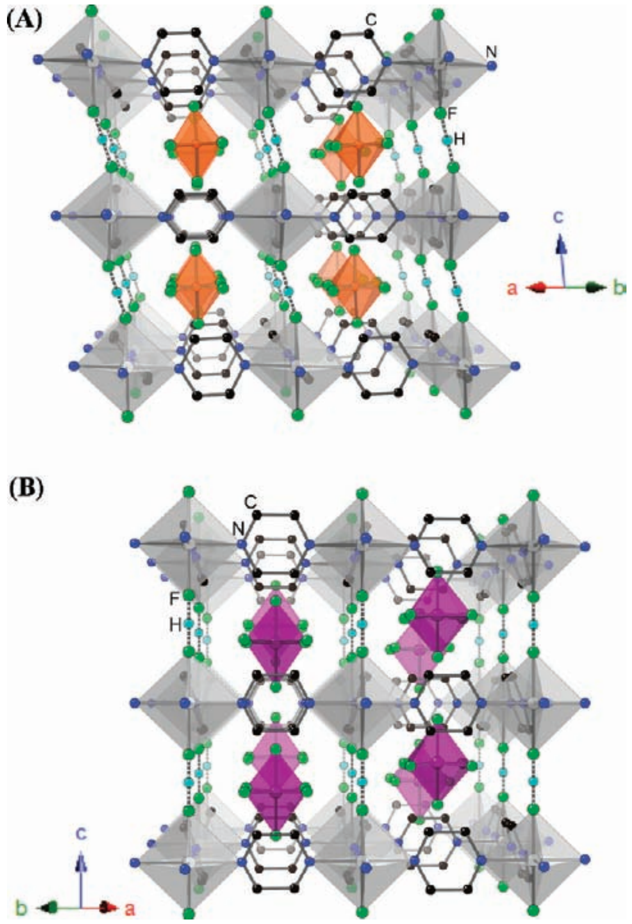

Figure 6. Polyhedral representations of the 3D coordination polymers: (A) $[Ni(HF_2)(pyz)_2]PF_6$ (**1**) and (B) $[Ni(HF_2)(pyz)_2]SbF_6$ (**2**). The figures pertain to 298 K structures. NiN_4F_2 and ZF_6^- octahedra are colored gray and orange (Z = P) or purple (Z = Sb), respectively. For the sake of clarity, pyrazine H's are not shown. Dashed cylinders delineate strong H···F hydrogen bonds.

antiferromagnetic couplings and ZFS. It should be pointed out that it is unrealistic to presume that ZFS alone is responsible for the observed magnetic behavior.

Evidence for a possible magnetic phase transition appears in a plot of $d\chi T/dT$ vs T (Figure 7b). A sharp λ-like peak is observed with a maximum exhibited at 6.2 K that we will designate as T_N. Approaching T_N from above, $d\chi T/dT$ rises slowly and then increases rapidly which may hint at some low dimensional spin correlations in the material. Repeating measurements of the low temperature magnetization (between 2 and 25 K) in external magnetic fields of 5, 7.5, 10, and 13 *T* shows a significant *B*-dependence of the λ-peak. Plots of $d\chi T/dT$ vs T for each of these data show that the peak temperature and its magnitude decrease with increasing *B*. This behavior is an earmark for long-range antiferromagnetic order, and a partial *B*/*T* phase diagram is shown as an inset in Figure 7b.

3.5. Magnetic Susceptibility of $[Ni(HF_2)(pyz)_2]SbF_6$ (2). In contrast to the broad maxima observed in the structurally related $[Cu(HF_2)(pyz)_2]X$ compounds, **2** shows a gradual rise in χ vs T (Figure 8a, main) until a "shark fin-like" rounded maximum (χ_{max} = 0.0250 emu/mol) is reached at 15 K which occurs at a temperature nearly twice as high as that found for **1**. Below T_{max}, the magnetic susceptibility decreases very rapidly and achieves a minimum value of 0.0184 emu/mol at 2 K. The rounding of the maximum may be due to single-ion (or exchange anisotropy) or the polycrystalline nature of the sample used in the measurement. For the sake of comparison, the crystal field experienced by the Ni(II) ions in **2** and K_2NiF_4 are somewhat similar. For K_2NiF_4, it has been reported that the weak tetragonal distortion gives rise to a small uniaxial anisotropy on the order of 10^{-3}.[51] A similarly small anisotropy may be anticipated for **2**.

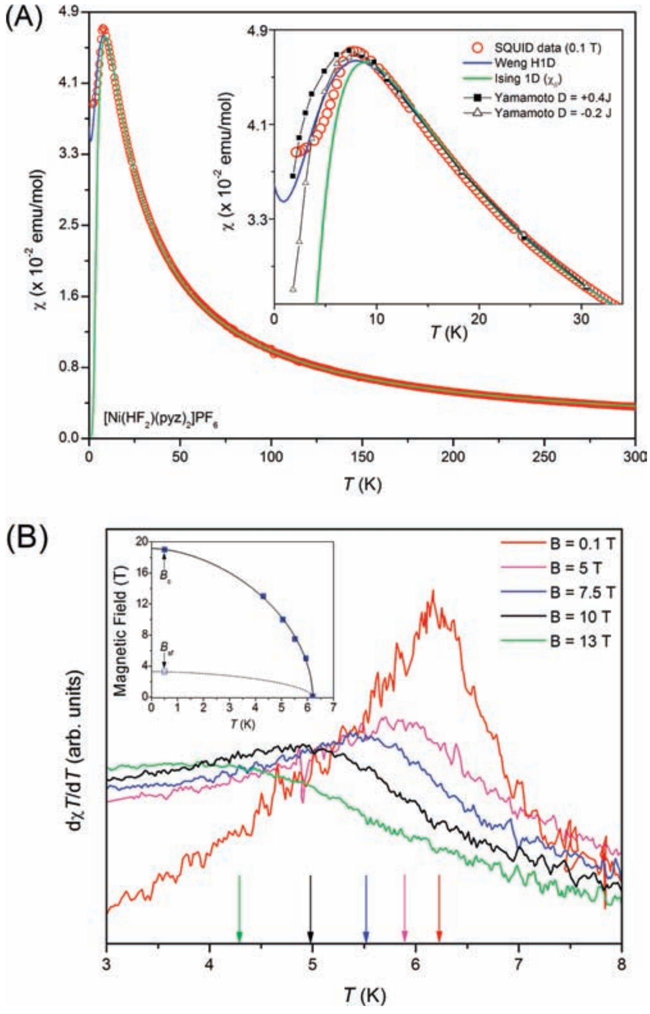

Figure 7. (A) Main plot: Magnetic susceptibility data (red open circles) for polycrystalline $[Ni(HF_2)(pyz)_2]PF_6$ (**1**). The solid lines denote theoretical fits of the χ vs T data to 1D Heisenberg and Ising models where g/J_{1D} = 2.05/3.05 K and 2.00/3.42 K, respectively. Inset plot: Low temperature susceptibility in the region around T_{max}. (B) Main plot: magnetic susceptibility data obtained for various external magnetic fields between 0.1 and 13 T. The estimated peak centers are highlighted by the colored arrows. Inset plot: Proposed *B*/*T* phase diagram for $[Ni(HF_2)(pyz)_2]PF_6$ (**1**). B_c and B_{sf} were determined by pulsed-field magnetization data at *T* = 1.43 K (see Figure 9). The solid and dashed lines serve only as guides to the eye.

A plot of $1/\chi$ vs T (Supporting Information, Figure S2) is linear between 60 and 298 K and was fitted to a Curie–Weiss law to give an average Landé *g*-factor of 2.081(1) and a Weiss constant (θ) of $-21.42(2)$ K, which indicates moderate antiferromagnetic correlations between $S = 1$ Ni(II) centers. Expectedly, the *g*-value exceeds the free electron value of 2.0023 but

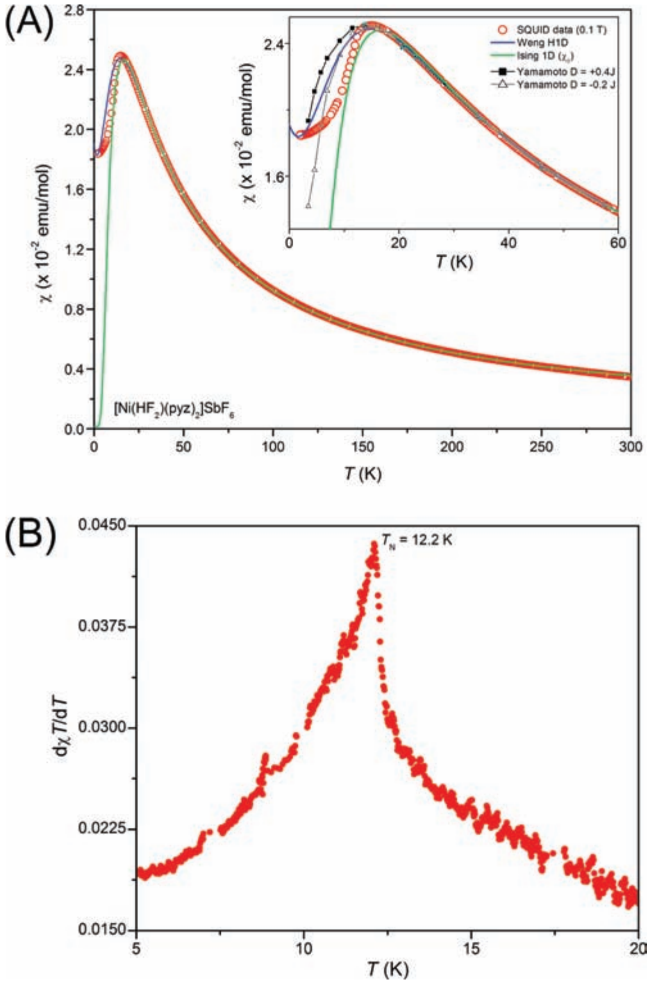

Figure 8. (A) Main plot: Magnetic susceptibility data (red open circles) for polycrystalline $[Ni(HF_2)(pyz)_2]SbF_6$ (**2**) measured in a 0.1 T dc field. The solid lines represent theoretical fits of χ vs T to 1D Heisenberg and Ising models using the g/J_{1D} parameters 2.06/5.65 K and 2.02/6.37 K, respectively. Inset plot: Low-T susceptibility around T_{max}. (B) $d\chi T/dT$ vs T for **2**.

is within an acceptable range and comparable to many other octahedral Ni(II) systems. The χT vs T plot for **2** is similar to that of **1** although the presence of stronger antiferromagnetic couplings is readily apparent.

A plot of $d\chi T/dT$ vs T (Figure 8b) reveals a λ-like peak at 12.2 K for **2** which is attributed to the onset of long-range magnetic order (T_N) in the material. The critical ratio T_N/θ can be used (*a priori*) to estimate the anisotropy of the spin interactions in a magnetic solid, and for **2**, this ratio is 0.57 which is substantially less than the value of 0.721 expected for an $S = 1$ 3D simple cubic Heisenberg antiferromagnet.[52] To date, $KNiF_3$ ($T_N/\theta = 0.716$) is the closest realization of the $S = 1$ 3D nearest-neighbor only Heisenberg system,[53] wherein each Ni(II) center is surrounded by six equidistant F^- ions.[54] The reduced T_N/θ ratio for **2** implies an exchange anisotropy among the Ni-pyz-Ni and Ni-FHF-Ni pathways which is consistent with DFT calculations (see below) and other observations. Unlike a simple 3D Heisenberg antiferromagnet where $T_{max} = 1.05T_N$,[55] T_{max} for **2** is $1.22T_N$ which suggests a reduction in spin dimensionality.

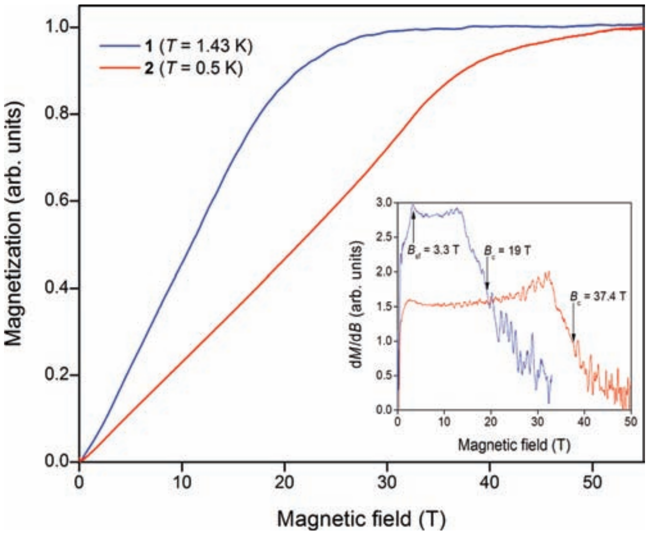

Figure 9. Main plot: Isothermal magnetization for $[Ni(HF_2)(pyz)_2]PF_6$ (**1**) and $[Ni(HF_2)(pyz)_2]SbF_6$ (**2**) acquired well below their respective T_N's of 6.2 and 12.2 K. Inset plot: dM/dB for **1** and **2** showing the various field-induced phase transitions. The low-field dM/dB anomaly for **2** is an extrinsic effect and is a consequence of the 111-point adjacent averaging algorithm used to calculate the curve.

3.6. Pulsed-Field Magnetization. Using polycrystalline samples of **1** and **2**, the isothermal magnetization M vs B was measured between 0.5 and 10 K and is shown in the main plots of Figure 9. As B increases, both compounds exhibit a slow initial rise in M which gradually increases slope (i.e., has a concave shape) until the critical field (B_c) is approached. At $T = 0.5$ K, $B_c \approx 19$ and 37.4 T for **1** and **2**, respectively, as defined by the midpoint between the peak in dM/dB and the region where dM/dB remains essentially constant (Figure 9, inset).[56] For **1**, a low field anomaly at ~3.3 T also occurs which is attributed to a field-induced spin-flop transition (B_{sf}) which is absent in **2**. Because B_{sf} is relatively large in **1**, we anticipate the anisotropy field (B_{anis}) to be ~0.28 T based on the mean-field relation, $B_{anis} \approx B_{sf}^2/2B_c$.[57] It is well understood that a spin-flop transition arises from an Ising-like anisotropy.[57]

The rounded nature of M in the vicinity of B_c could be due to several reasons including the powdered nature of the samples, a sizable zero-field splitting, and/or substantial interchain couplings. A concave shape of M vs B is known to be a strong indication of significant exchange anisotropy in $S = 1/2$ systems. We find that the low field magnetization exhibited by **1** and **2** also feature a marked concavity that is similar, although less pronounced, than that found in $[Cu(HF_2)(pyz)_2]X$ ($X = PF_6^-$ and SbF_6^-).[9,10] The reduction in concavity is likely due to the increased value of the spin quantum number in the Ni(II) systems. For both **1** and **2**, B_c broadens and shifts to lower magnetic fields as the temperature increases; the concavity of M vs B gradually disappears and the curve becomes more Brillouin-like.

3.7. Long-Range Magnetic Order in $[Ni(HF_2)(pyz)_2]PF_6$ (1) and $[Ni(HF_2)(pyz)_2]SbF_6$ (2). While there is convincing evidence for the occurrence of long-range magnetic order in **1** and **2** we sought to independently verify this possibility using complementary experimental probes, namely, muon-spin relaxation and specific heat. μSR is uniquely sensitive to spin dynamics and phase transitions in small magnetic moment systems and has

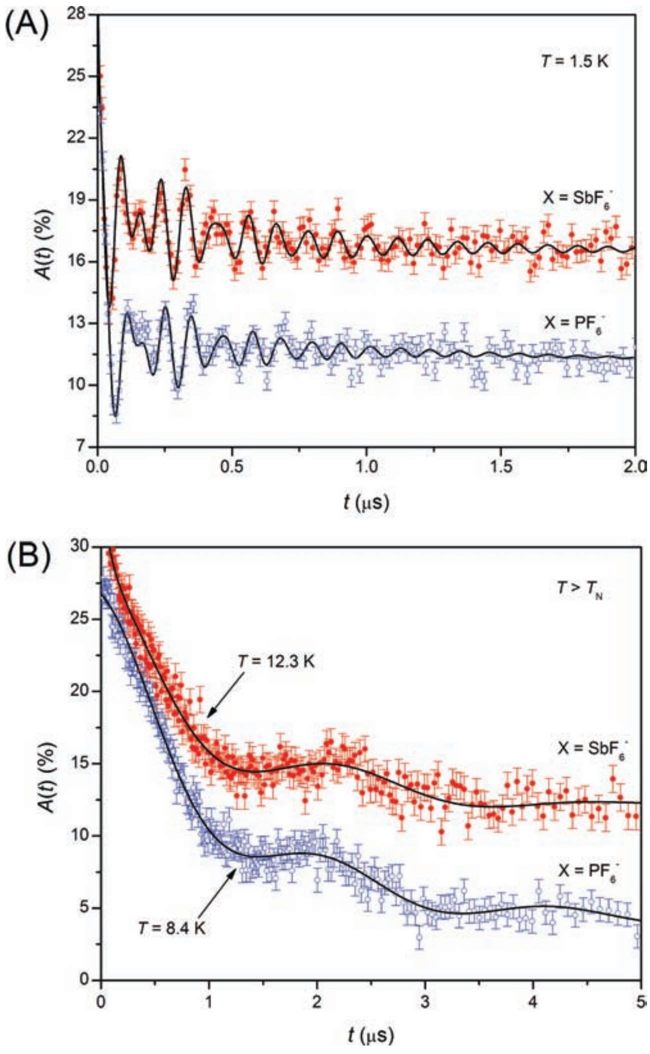

Figure 10. (A) Muon asymmetry spectra, $A(t)$, for **1** and **2** at T = 1.5 K which is well below T_N. Solid lines are fits of the data to eq 2. (B) The $A(t)$ spectra above T_N have a different character and display slow oscillations indicative of F-μ dipole−dipole interactions.[58c]

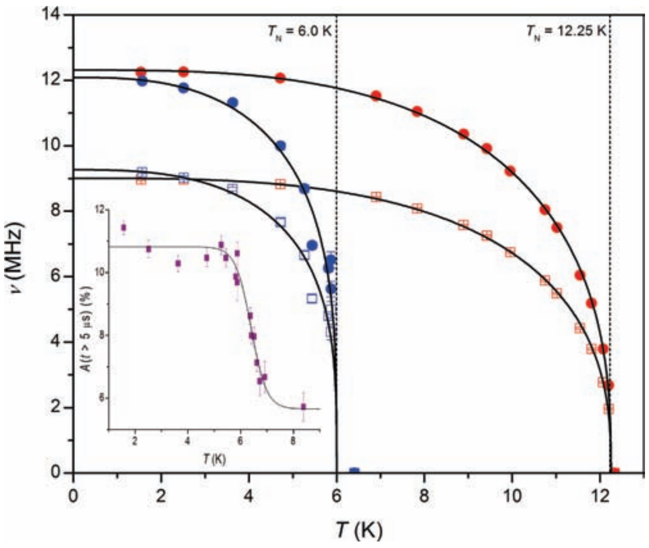

Figure 11. Main plot: Muon-spin precession frequencies (ν) as a function of temperature for **1** and **2**. Solid lines represent power law fits of the data. For most of the data points, error bars are smaller than the symbol size. Compound **2** has the higher magnetic ordering temperature. Inset plot: The change in amplitude at late times as a function of temperature for **1** as described in the text. The fitted line originates from eq 3.

proven to be invaluable in our investigation of low-dimensional Cu(II) quantum magnets, and we apply both methods in this work.[6,7,10,58]

3.7.1. Muon-Spin Relaxation Studies. Asymmetry spectra for **1** and **2** are shown in Figure 10 above and below the transition. Two frequencies and a very fast initial relaxation are visible in the spectra below T_N, indicative of three classes of magnetically inequivalent muon stopping sites. The precession frequencies, ν_i, decrease as the transition is approached from below, as shown in Figure 11.

Data taken on **2** at 1.5 K were fitted with a relaxation function (eq 2),

$$A(t) = A_0[p_1 \cos(2\pi\nu_1 t)e^{-\lambda_1 t} + p_2 \cos(2\pi C_2 \nu_1 t)e^{-\lambda_2 t} + p_3 e^{-\lambda_3 t}] + A_{bg}e^{-\lambda_{bg} t} \qquad (2)$$

where A_{bg} is the amplitude of a slowly relaxing component which includes a contribution from those muons that stop in the silver sample holder or cryostat tails. Of those muons that stop in the sample, the parameter $p_1 \approx 10\%$ gives the weighting of the measured asymmetry from an oscillating component with $\nu_1(T = 0) \approx 9.0$ MHz; $p_2 \approx 25\%$ from a higher frequency oscillating component with $\nu_2(T = 0) \approx 12.3$ MHz; and $p_3 \approx 65\%$ is the weighting of a component reflecting muon sites whose fluctuating local fields give rise to a large relaxation rate $\lambda_3(T = 0) \approx 70$ MHz. The second frequency was held in fixed proportion, $\nu_2 = C_2\nu_1$, during the fitting routine, where $C_2 = 1.37$.

The only other parameter which changes significantly in value below T_N is λ_3, which decreases with a trend qualitatively similar to that of the muon precession frequencies. This suggests that this relaxation rate is governed primarily by the magnitude of the internal magnetic field in the material. Relaxation rates are expected to vary as $\lambda \propto \Delta^2\tau$,[59] where Δ is proportional to the second moment of the local magnetic field distribution and τ is its fluctuation time. Since $\Delta \propto \nu$, we might expect $\lambda \propto \nu^2$; this relation holds approximately true. Fitting frequency against temperature with a power law, $\nu(T) = [1 - (T/T_N)^\alpha]^\beta$, allows the transition temperature $T_N = 12.25(3)$ K and critical exponent $\beta = 0.34(4)$ to be extracted. The extracted β-value is consistent with the 3D Heisenberg ($\beta = 0.367$) or 3D *XY* ($\beta \sim 0.33$) model of critical behavior.[60] It is important to note that β is highly sensitive to the value of T_N as evidenced by the relatively large uncertainties in both parameters.

A similar analysis was applied to **1**, fitting spectra below T_N to eq 2, this time with $p_1 \approx 10\%$, $\nu_1(T = 0) \approx 9.3$ MHz; $p_2 \approx 15\%$, $\nu_2(T = 0) \approx 12.1$ MHz; and $p_3 \approx 75\%$, $\lambda_3(T = 0) \approx 100$ MHz and the constant of proportionality relating the frequencies was fixed at $C_2 = 1.30$. Graphs of example spectra and fitted frequencies can be seen in Figure 10.

These spectra do not show as sharp a transition as they do in **2**, with the oscillating fraction of the signal decaying rather before the appearance of spectra whose different character indicates clearly that the sample is above T_N. Naively fitting the frequencies as a function of temperature yields critical behavior that does

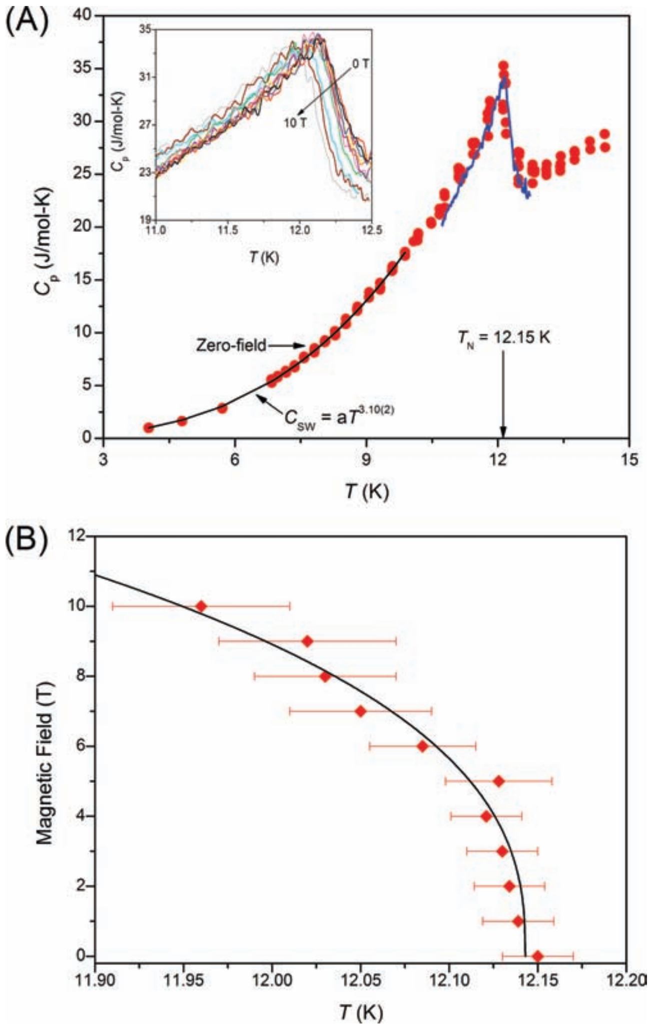

Figure 12. Specific heat of polycrystalline $[Ni(HF_2)(pyz)_2]SbF_6$ (**2**). (A) Main plot: zero-field data collected using traditional (solid circles) and dual-slope (solid line) relaxation methods. The black line is a fit to the spin wave expression $C_{SW} \propto T^{d/n}$. Inset plot: Field-dependence of the specific heat taken between zero and 10 T using the dual-slope technique. (B) Partial phase diagram as determined by the specific heat data. The large temperature errors are due to the breadth of the λ-peak observed at each field interval. The line is a guide to the eye only.

not correspond with conventional models, but manually constraining $5.5 \leq T \leq 6.2$ K fits to $0.15 < \beta < 0.4$ rendered it impossible to reliably relate the critical behavior to a particular theoretical model.

Another method to locate the magnetic phase transition is to observe the amplitude of the muon spectra at long times. In a polycrystalline sample in the quasistatic limit, the 1/3 of the muons whose spin direction is parallel with the local magnetic field will not relax, remaining pinned along the field direction. This gives rise to a nonzero amplitude tail in the spectra at late times. However, the presence of dynamic fluctuations flattens this tail, and the muon asymmetry will relax to zero. Below the magnetic ordering transition, muons are sensitive to large, quasistatic B-fields from the large, ordered electronic moments, giving rise to a 1/3-tail. However, above T_N, dynamic fluctuations of the electronic spins depolarize all muons. The transition can thus be located by fitting the asymmetry at late times as a function of temperature to monitor the disappearance of this tail.

Spectra were fitted with the simple relaxation function $A(t > 5\ \mu s) = A_{bg}e^{-\lambda_{bg}t}$, and then the amplitudes obtained were fitted with a Fermi-like step function (eq 3),

$$A(t > 5\ \mu s, T) = A_2 + \frac{A_1 - A_2}{e^{(T - T_N)/w} + 1} \qquad (3)$$

which experiences a transition between $A_1 = A(T < T_N)$ and $A_2 = A(T > T_N)$. The fitted amplitudes and step function are shown in the inset of Figure 11. The fitted midpoint T_N = 6.4(1) K and width w = 0.3(1) K. In estimating T_N from this method, whether to use the onset, midpoint, end, or another point of this amplitude transition would require a nontrivial analysis of the material's critical dynamics; nonetheless, the lower end of this transition appears consistent with the estimate from $\nu_i(T)$ and T_N = 6.2 K as obtained from magnetization measurements. The μ^+SR analysis suggests that T_N = 6.0(4) K for **1**.

*3.7.2. Specific Heat Studies on $[Ni(HF_2)(pyz)_2]SbF_6$ (**2**).* A polycrystalline sample of **2** was studied using the heat-pulse and dual-slope thermal relaxation methods. Major advantages of the dual-slope method are rapid data collection and improved sensitivity. The main panel of Figure 12a compares the zero-field specific heat (C_p) result obtained using both techniques where it can be seen that good reproducibility is achieved. A broadened λ-like anomaly centered at 12.2 K was observed using both relaxation methods. This feature is coincident with the sharp anomaly seen in the $d\chi T/dT$ vs T plot (see Figure 8b). We mention that in the case of a single crystal with its easy-axis aligned parallel to B, Fisher showed that a peak in $d\chi T/dT$ vs T occurs at the Néel temperature; such a peak was found in our data despite the polycrystalline nature of our sample.[55] For $T < T_N$, C_p can be fitted to the relation, $C_{sw} \propto T^{d/n}$, with d = 3.10(2) and n = 1. The d-value obtained from the low-T fit is very close to the T^3-dependence expected for 3D antiferromagnetic spin waves.[61]

The limited temperature range of the measurement prevented our determination of the phonon contribution (C_{latt}) to the specific heat and thus extraction of the magnetic specific heat (C_{mag}) and magnetic entropy (ΔS_{mag}). Without subtraction of C_{latt} it is not possible to assess whether a Schottky anomaly precedes the λ-peak as expected for a quasi-1D magnetic system.

The inset of Figure 12a shows the field-dependence of the λ-like peak. As the external field is progressively increased, it can be seen that the peak maximum temperature actually decreases. Such behavior is expected of an ordered 3D antiferromagnet.[61] Plotting the peak temperature and the associated magnetic field leads to the partial B/T phase diagram given in Figure 12b. The subtle change in width of the λ-peak and rather weak field-dependence leads to the observed temperature errors.

4. DISCUSSION

4.1. Effect of Temperature on NiN_4F_2 Geometry. At 17 K, the unit cell volumes of **1** and **2** decrease by 1.7% and 1.0%, respectively, as compared to 298 K data. Although V does not change appreciably with temperature, the Ni−F, Ni−N, and H−F bond lengths do exhibit significant variations as evident from Tables 3 and 4. For both **1** and **2**, the Ni−F bond lengths shorten to 1.98 Å (PF_6^-) and 2.07 Å (SbF_6^-). However, the Ni-pyz bonds in **1**, Ni−N1 and Ni−N2, expand to 2.19 and 2.20 Å. For **2**, the Ni−N bond contracts to 2.10 Å. The H···F bonds in both compounds lengthen slightly and the F···H···F bond angle in **1** decreases to 152° whereas the corresponding angle in **2** remains linear. Internal N−Ni−F bond angles also experience increased rhombic distortion in **1** which is accompanied by drastic changes in molecular geometry of the PF_6^- counterion. At low temperatures, the NiN_4F_2 site in **1** is much more distorted than in **2**.

4.2. Intra- and Interchain Magnetic Couplings in [Ni(HF_2)(pyz)$_2$]X. The drastic decrease in the magnetic susceptibilities below T_{max} for **1** and **2** might be explained in several ways. First, the ground state of the Ni(II) ion could be a nonmagnetic singlet originating from the exchange interaction and the ZFS. Second, an Ising system is present although $g_{\|}$ must be much larger than $g_{\perp}$ to induce the large decrease in the powder susceptibility; however, the *g*-factor anisotropy is typically quite small for Ni(II) ions in an octahedral environment. Third, an axial and/or rhombic zero-field splitting (*D*) of the Ni(II) ion is likely to be important. Fourth, an anisotropic exchange coupling exists.

Considering that the known square lattices based on $[Ni(pyz)_2]^{2+}$ units show only weak intralayer Ni-pyz-Ni magnetic exchange and that none of them exhibit long-range magnetic order above 2 K, it is reasonable to assume that the dominant contributor to the total spin exchange is along Ni-FHF-Ni pathways. Hence, we will describe the magnetic lattice of **1** and **2** as quasi-1D Ni-FHF-Ni linear chains arranged on a tetragonal lattice (i.e., an anisotropic cubic lattice) with four nearest-neighboring chains that are separated by pyz bridging units. This will give intrachain J_{1D}/k_B (hereafter denoted J_{1D}) and interchain $J_{\perp}/k_B$ (hereafter denoted $J_{\perp}$) interactions according to the spin Hamiltonian (eq 4),

$$\hat{H} = J_{1D}\sum_{\langle i,j\rangle z} S_i\cdot S_j + J_{\perp}\sum_{\langle i,j\rangle xy} S_i\cdot S_j + D\sum_{i}(S_i^z)^2 \qquad (4)$$

where positive J_{1D} and $J_{\perp}$ values represent antiferromagnetic interactions between Ni(II) spin carriers and *D* is the ZFS that arises from the expected single-ion anisotropy of Ni(II). We caution that the inherent averaging involved in powdered samples limits the extent to which we can draw conclusions regarding *D* solely based on susceptibility data. Because single crystals of **1** and **2** are currently unavailable it is not possible to deconvolute the parallel and perpendicular susceptibilities as needed to properly evaluate the sign and magnitude of *D*. However, various magnetic models are available, which are typically used to extract the primary exchange parameter (i.e., the first term) of the spin Hamiltonian using high-temperature magnetic susceptibility data above T_{max}. In this work, we compare the relevant theoretical models based on uniform $S = 1$ 1D chains, that is, Heisenberg (Weng[62] and Meyer and coworkers[63]) and the parallel susceptibility ($\chi_{||}$) of the Ising system (as applied to $CsNiCl_3$ by Smith and coworkers[64]). The results of least-squares fits over the range $T_{max} < T < 298$ K, which are extrapolated to $T = 0$, are shown collectively in Figures 7a and 8a for **1** and **2**, respectively. The resulting g/J_{1D} fit parameters are 2.05/3.05 K (**1**) and 2.06/5.65 K (**2**) (Heisenberg) and 2.00/3.42 K (**1**) and 2.02/6.37 K (**2**) (Ising). Regardless of the model used it is clear that the results are somewhat ambiguous as each model yields good agreement with the data above T_{max}. Below T_{max} these models fail to reproduce the experimentally observed behavior.

Yamamoto and Miyashita[65] recently reported the thermodynamic properties of the infinite chain $S = 1$ Heisenberg model and computed a range of the anisotropy D/J_{1D} for the parallel and perpendicular susceptibilities. We combined these curves in the usual way to obtain the powder average susceptibility. Scaling their results to our susceptibility data afforded the curves (with Δ and ■ corresponding to the extremes $D = -0.2J$ and $+0.4J$, respectively) also shown in Figures 7a and 8a. The best match of the calculated curves to our data occurs for $J_{1D} = 3.05$ K (**1**) and 5.75 K (**2**). Qualitative agreement is achieved for temperatures close to the maximum; however, significant deviations are found below T_{max} which may suggest the need for a larger D/J_{1D} ratio. The fact that none of the aforementioned models adequately explain the low-*T* behavior presumably reflects the presence of more complex physics for which a complete model has not yet been identified. It is possible that these effects could originate from a Haldane phase, although its presence is not supported by the pulsed-field magnetization or μSR. If indeed the D/J_{1D} ratio is close to 1, then the primary interaction energy extracted from the fits to the various models in Figures 7a and 8a above the broad hump, rather than reflecting the magnitude of J_{1D} alone, is in fact representative of a combination of J_{1D} and *D* terms in the spin Hamiltonian, which together give rise to the form of the susceptibility across this temperature range. Furthermore, although it is not possible to experimentally isolate the interchain $J_{\perp}$ term, it is evident that it must be sufficient enough to support long-range antiferromagnetic order at the relatively high values of T_N that are observed for **1** and **2**.

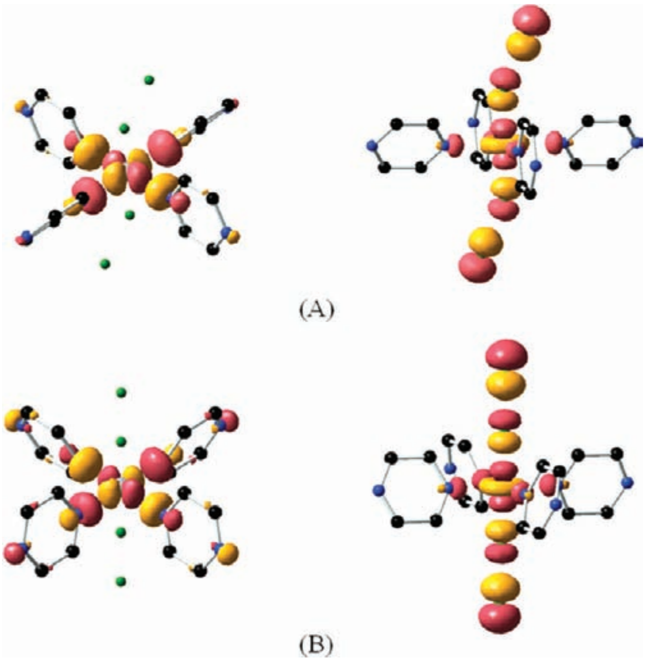

Figure 13. Ni(II) $3d_{x^2-y^2}$ (left) and $3d_{z^2}$ (right) magnetic orbitals as found in (A) $[Ni(HF_2)(pyz)_2]PF_6$ (**1**) and (B) $[Ni(HF_2)(pyz)_2]SbF_6$ (**2**) as deduced from DFT analysis of $Ni(HF_2)_2(pyz)_4$ octahedra based on the B3lyp functional and 3-21G* basis set.

4.3. DFT Evaluation of Ni···Ni Spin Exchange Interactions. Each Ni(II) ion in $[Ni(HF_2)(pyz)_2]X$ {pyz = pyrazine; X = PF_6^- (**1**), SbF_6^- (**2**)} has two magnetic orbitals, as depicted in Figure 13, which were obtained by performing DFT calculations for isolated octahedral clusters of $Ni(HF_2)_2(pyz)_4$ (based on 298 K structural data) with the B3LYP exchange correlation functional[66−68] and the 3-21G* basis functions encoded in the Gaussian 03 B.04 program package.[69] Provided that the local

Table 5. Values of the Antiferromagnetic Spin Exchange Parameters, $J_\perp$ and J_{1D}, as Obtained from the GGA+U Calculations with $U = 4$ eV. The Respective $\angle$Ni···N···N and $\angle$Ni···F···F Bond Angles of the Ni-pyz-Ni and Ni-FHF-Ni Exchange Pathways in 1 and 2 are Also Listed

		X = PF_6^-	X = SbF_6^-
Ni-pyz-Ni	$J_\perp/k_B$	2.5 K	9.2 K
	$\angle$Ni···N···N	175.4, 177.2°	180.0°
Ni-FHF-Ni	J_{1D}/k_B	12.7 K	19.7 K
	$\angle$Ni···F···F	156.2°	180.0°

z-axis is taken along the Ni-FHF-Ni path with the local x and y axes along the Ni-pyz-Ni paths, these magnetic orbitals have $d_{x^2-y^2}$ and d_{z^2} character. The $d_{x^2-y^2}$ orbital is involved in the Ni-pyz-Ni spin exchange ($J_\perp$) in the *ab*-plane, and the d_{z^2} orbital in the Ni-FHF-Ni spin exchange (J_{1D}) along the *c*-axis. The Ni-FHF-Ni and Ni-pyz-Ni exchange paths are linear in **2** but are bent in **1** (see Table 5 for the $\angle$Ni···N···N angles of the Ni-pyz-Ni paths and the $\angle$Ni···F···F angles of the Ni-FHF-Ni paths).

As illustrated in Figure 14, the Ni-FHF-Ni spin exchange path consists of stronger σ-overlap between the Ni d_{z^2} and the F sp orbitals of FHF^- for **2** than for **1** so that the Ni-FHF-Ni spin exchange should be stronger for **2**. The Ni-pyz-Ni spin exchange involves σ-overlap between the $d_{x^2-y^2}$ and the N sp^2 orbitals of pyz so that the Ni-pyz-Ni spin exchange should be stronger for **2** than for **1**. Furthermore, the $d_{x^2-y^2}$ orbital overlaps with four pyz ligands while the d_{z^2} orbital overlaps mainly with two FHF^- ligands, such that the weight of each ligand is greater for the d_{z^2} orbital than for the $d_{x^2-y^2}$ orbital.

To evaluate the Ni-pyz-Ni and Ni-FHF-Ni spin exchanges of **1** and **2**, we consider three possible ordered spin states and determine their relative energies by performing GGA+U calculations (see Supporting Information, Figures S3 and S4). Excluding the ZFS term in eq 4, a more simplified Hamiltonian was employed. By mapping the relative energies of these states determined from the GGA+U calculations onto the corresponding relative energies determined from the spin Hamiltonian,[70] we obtained the values of J_{1D} and $J_\perp$ as summarized in Table 5. We note that the spin exchanges obtained by GGA+U calculations are typically overestimated by a factor of up to 4 as compared to experimentally derived values.[71] However, the relative exchange constants are well described by the GGA+U calculations. The calculated J_{1D} and $J_\perp$ values confirm our suggestions emerging from the magnetic orbitals shown in Figures 13 and 14. For **1** and **2**, the Ni-FHF-Ni exchange J_{1D} is stronger than the Ni-pyz-Ni exchange $J_\perp$. Subsequently, J_{1D} and $J_\perp$ are stronger for **2** than for **1** because the Ni-FHF-Ni and Ni-pyz-Ni configurations are linear in the former but distorted in the latter.

Considering the DFT established J_{1D} and $J_\perp$ parameters, we calculate the respective critical $J_\perp/J_{1D}$ ratios for **1** and **2** to be 0.20 and 0.47. These ratios reflect the reduced spin dimensionality of these compounds and the more pronounced 1D magnetic character of **1** and are in line with their observed structural differences. In more ideal 1D Ni(II) chains, the $J_\perp/J_{1D}$ ratios are typically much smaller, for example, 7×10^{-2} and 7×10^{-3} for $RbNiCl_3$ and $CsNiCl_3$, respectively.[72,73]

4.4. Estimation of the ZFS. It is well-known that the lowest energy state of a Ni(II) complex with ideal O_h symmetry is an orbital singlet $^3A_{2g}$.[36] The spin degeneracy of the $^3A_{2g}$ state is removed by the combination of spin–orbit coupling and a reduced (i.e., noncubic) local symmetry. Under a tetragonal crystal field, spin–orbit coupling connects the tetragonal split components of the excited $^3T_{2g}(O_h)$ and $^3T_{1g}(O_h)$ states to the spin components of the $^3B_{1g}(D_{4h})$ ground state. A large difference between axial and equatorial ligand fields induces significant splitting of the aforementioned excited states and can lead to a large ZFS. This is to say that the $m_s = \pm 1$ spin doublet of the ground state is coupled to the $^3E_g(D_{4h})$ orbital doublet of the first excited state. In turn, the $m_s = 0$ spin singlet is connected to the $^3B_{2g}(D_{4h})$ state (i.e., second excited state). Should the axial ligand field be weaker than the equatorial ligand field, then the $^3E_g(D_{4h})$ level will be lower in energy than the $^3B_{2g}(D_{4h})$ level, thus giving $D > 0$. Conversely, if the $^3E_g(D_{4h})$ level is higher in energy relative to $^3B_{2g}(D_{4h})$, then $D < 0$ is expected.

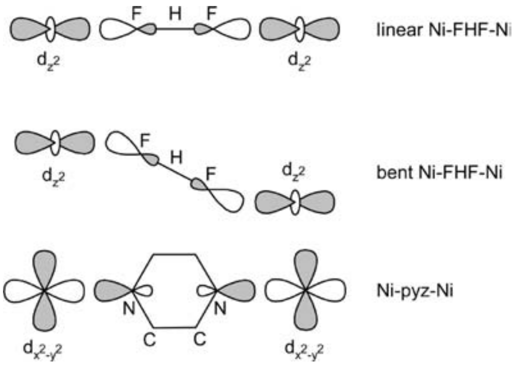

Figure 14. Schematic diagrams illustrating the orbitals involved in the Ni-FHF-Ni and Ni-pyz-Ni spin exchange paths of **1** and **2**. The Ni-FHF-Ni exchange involves σ-overlap between Ni d_{z^2} and F sp orbitals of FHF^- whereas the Ni-pyz-Ni exchange involves overlap between Ni $d_{x^2-y^2}$ and N sp^2 orbitals of pyz. The reduced σ-overlap between F sp and Ni d_{z^2} orbitals is readily apparent in the bent Ni-FHF-Ni configuration, thus enhancing the π-donor ability of the HF_2^- ligand.

On the basis of the spectrochemical series, fluoride is predicted to be a weaker field ligand than typical amines (e.g., pyrazine); however, unlike F^-, the bond character of HF_2^- bears some covalency.[74] Not only are the electronic properties of the ligands important, but the ligand field strength and orbital mixing (covalency) also strongly depend on the spatial distribution of the ligating atoms. In **1**, the significant geometrical distortion (axial compression plus slight rhombicity) appears to overrule the conventional ordering of the ligating atoms in terms of ligand field strength; the NiN_4F_2 chromophore in **2** is less distorted. Considering all these factors allows us to estimate the *D*-value based on the electronic transitions observed in *room temperature* absorption spectra (cf. sect. 3.2). To complement the current study, low temperature UV–vis data are needed in light of the apparent distortions of the NiN_4F_2 sites.

Using a crystal field derivation (eq 5),[75] it has been shown that D can be determined by the excitation energies $\Delta_{xy}(^3E_g \leftarrow {}^3B_{1g})$ and $\Delta_z(^3B_{2g} \leftarrow {}^3B_{1g})$, the orbital reduction factor (κ), and the single-electron spin–orbit coupling constant (ζ):

$$D = 4\left(\frac{\zeta}{2S}\right)^2\left(\frac{\kappa_{xy}^2}{\Delta_{xy}} - \frac{\kappa_z^2}{\Delta_z}\right) \qquad (5)$$

The interpretation of the spectra in sect. 3.2 combined with the geometric tetragonal compression found in **1** requires that $\Delta_z < \Delta_{xy}$. Provided that κ_z and κ_{xy} are similar, this will yield $D < 0$. For **2**, on the other hand, the near-perfect octahedral

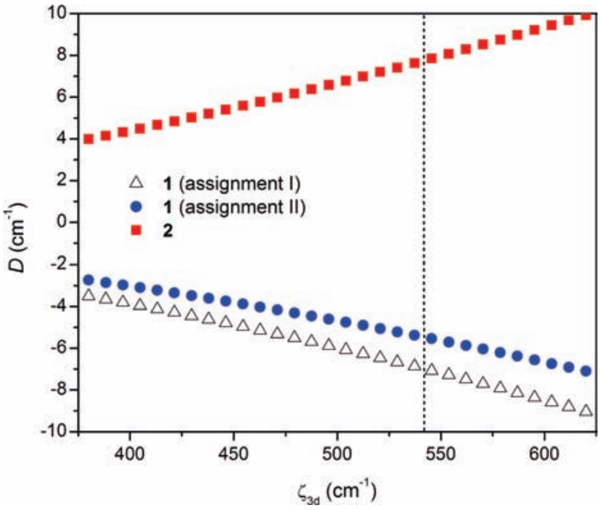

Figure 15. Axial zero-field splitting (D) calculated as a function of the one-electron spin–orbit coupling parameter (ζ), using the optimized AOM parameters (Sect. 3.2). For **1** the actual coordination geometry was employed for both alternative assignments. For **2** the orthoaxial geometry was used in concordance with the structural data. The dashed vertical line corresponds to a spin–orbit coupling parameter reduced from the free-ion value by the same factor as the Racah B parameter, which is well determined from the 298 K electronic absorption spectra.

geometry and the spectral analysis suggest $\Delta_{xy} < \Delta_z$ so that $D > 0$ is more plausible. This electronic configuration for **2** is generally consistent with an axial weakening.

Depending on the nature of the coordinating ligands, ζ can vary over a wide range of values (375–640 cm^{-1} as compared to the free-ion value of 668 cm^{-1}) and be anisotropic for heteroleptic complexes.[38d,39] Utilizing this range of ζ-values and the corresponding excitation energies, $|D|$ is estimated from eq 5 to lie between 3.5 and 9.0 cm^{-1} (assignment I) or 2.8–7.0 cm^{-1} (assignment II) for **1** and 4.0–10.0 cm^{-1} for **2**. Realistically, κ_z and κ_{xy} will vary (and be less than unity) because the degree of covalency of the interaction with equatorial and axial ligands is different. The nephelauxetic ratios, as determined from the fitted values of B (847–861 cm^{-1}), yield $B/B_{free\text{-}ion} = 0.81–0.83$ which can be directly compared to the aforementioned κ. A somewhat higher range of κ-values (0.91–0.96) have been reported for KNiF$_3$.[41] The lower values computed for **1** and **2** suggest enhanced covalency among the coordinate bonds owing to the distinctly different electronic structures of FHF$^-$ and pyz relative to predictably ionic F$^-$.

A better ligand-field estimate of D, taking into account all states of the d^8 electronic configuration, can be obtained by using the optimized AOM parameters determined from the UV–vis absorption spectra in conjunction with the aforementioned range of ζ-values. A plot of $\pm D$ vs ζ for the assignments used in Sect. 3.2 is given in Figure 15. Again, negative and positive D-values are predicted for **1** and **2**, respectively, owing to the different order of the $^3E_g(D_{4h})$ and the $^3B_{2g}(D_{4h})$ levels which coincides with the inversion of the $d_{x^2-y^2}$ and d_{z^2} orbitals as suggested by DFT. The dashed vertical line in Figure 15 corresponds to ζ of ~540 cm^{-1} which is reduced from the free-ion value by the same factor as the Racah B parameter; this gives $D = -6.6$ cm^{-1} (**1**, assignment I), -5.2 cm^{-1} (**1**, assignment II), and 7.8 cm^{-1} (**2**).

A survey of the numerous examples of six-coordinate Ni(II) coordination complexes that have known crystal structures has revealed a broad range of D-values of both positive and negative sign.[76] For instance, [Ni(HIM2-py)$_2$(NO$_3$)]NO$_3$ {HIM2-py = 1-hydroxyl-2-(2′-pyridyl)-4,4,5,5-tetramethyl-4,5-dihydro-1*H*-imidazole} possesses pseudo-C_{2v} symmetry and has a large D of -10.1 cm^{-1} ($g = 2.17$) as determined by magnetization data and frequency-domain magnetic resonance spectroscopy.[77] Elongated *trans*-NiO$_4$N$_2$ cores found in {Ni[C(CN)$_2$NO·MeOH](H$_2$O)$_2$}[78] and [Ni(CMA)$_2$(im)$_2$(H$_2$O)$_2$] (CMA = 9,10-dihydro-9-oxo-10-acridineacetate; im = imidazole)[79] lead to large positive D-values of 9.47 cm^{-1} and 5.6 cm^{-1}, respectively. Evidently, the sign of D may be more dependent on the electronic characteristics of the ligands rather than the type of axial distortion of the Ni(II) chromophore.

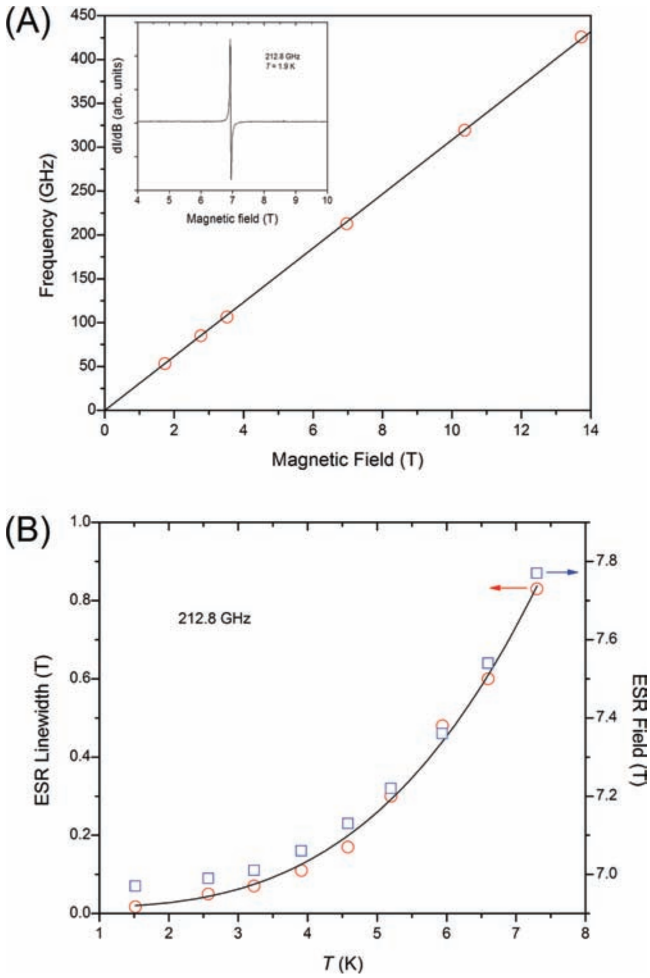

Figure 16. (A) Frequency-field dependence of magnetic excitations for [Ni(HF$_2$)(pyz)$_2$]SbF$_6$ (**2**) measured at T = 1.9 K. The inset shows a typical ESR signal at a frequency of 212.8 GHz and T = 1.9 K. (B) Temperature dependence of the resonance shift (squares) and ESR line width (circles) measured at a frequency of 212.8 GHz below T_N = 12.2 K. The line in (B) is a guide to the eye only.

4.5. Spin Dynamics. To obtain important information on the spin Hamiltonian parameters, powder samples of **1** and **2** were probed by means of high-field and high-frequency electron spin resonance. A thorough search for resonance absorption in **1** gave no indication for an antiferromagnetic resonance (AFMR) mode in contrast to **2**. In the ordered state of **2**, a linear frequency-field dependence of magnetic excitations was observed (Figure 16a), from which the slope corresponds to g = 2.21 (measured at

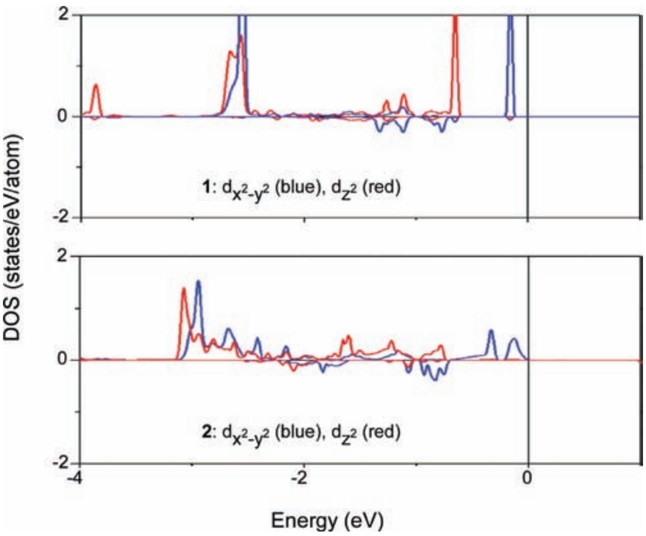

Figure 17. Projected density of states calculated for the d_{z^2} and $d_{x^2-y^2}$ states of **1** and **2**. The broader distribution of states in **2** indicates a greater spin delocalization along the Ni-FHF-Ni and Ni-pyz-Ni pathways as compared to **1** where the bands are more localized. In each diagram, the upper panel corresponds to up-spin states and the lower panel the down-spin states.

$T = 1.9$ K in the frequency range 50−440 GHz) as typical for an $S = 1$ Ni(II) ion.[80] Upon warming, the ESR line-width broadens and shifts toward higher magnetic fields (Figure 16b) which reflects a pronounced competition between long-range spin correlations and thermal fluctuations.[81] No ESR signal was observed above T_N, suggesting that the observed ESR absorption corresponds to AFMR excitations of a 3D-coupled network of Ni ions. Since no procedure for the analysis of AFMR spectra of a powdered Ni(II)-based antiferromagnet is available, we speculate that the lack of or presence of AFMR in **1** and **2**, respectively, may be due to different signs of the single-ion anisotropy in **1** ($D < 0$) and **2** ($D > 0$) as suggested by LFT. Also of interest is that the *g*-value of **2** as obtained below T_N is larger than the *g*-factor obtained from the fits of the high-temperature magnetic susceptibility; we suggest that this may be a consequence of the anisotropy that develops in the ordered state.[82]

4.6. Other Considerations. On the basis of 298 K structural and spectroscopic data, we suggest that $D < 0$ for **1** and $D > 0$ for **2** which implies that the $d_{x^2-y^2}$ magnetic orbital lies lower in energy than the magnetic d_{z^2} orbital for **1**, but this ordering is inverted in **2**. Our DFT calculations for the isolated octahedral clusters $Ni(HF_2)_2(pyz)_4$ taken from **1** and **2** confirm this implication if a small basis set (e.g., 3-21G*) is used, but predict that d_{z^2} lies lower than $d_{x^2-y^2}$ for both compounds if an extended basis set (e.g., LANL2DZ ECP for Ni and 6-31G* for C, N, F and H) is employed. Figure 17 shows the projected density of states calculated for the d_{z^2} and $d_{x^2-y^2}$ states of **1** and **2**. These states form broader bands in **2** relative to **1**, which reflects the fact that the magnetic d_{z^2} orbitals interact more strongly in **2** than in **1**, as do the magnetic $d_{x^2-y^2}$ orbitals.

In the various, albeit few, examples of quasi-1D and 2D Ni-pyz coordination polymers that have been reported, the Ni-pyz-Ni exchange interactions ($J_\perp$) are relatively weak as can be seen in Table 6.[83−87] Upon close inspection of these data, there is no apparent correlation between the type of ligand donor atoms, Ni−N bond lengths, pyrazine tilt angle, or dimensionality of the spin system. Another important aspect worthy of consideration may lie in the donor/acceptor properties of the coordinated ligands themselves and perhaps a correlation among Racah *B* parameters or other ligand field parameters may arise. For **1** and **2**, the difference in computed $J_\perp$ values may be linked to the rhombic distortion of the NiN_4F_2 center and bent Ni···N···N paths in **1** which reduces the effective σ-overlap between Ni $d_{x^2-y^2}$ and pyz lone-pair orbitals. However, J_{1D} for $Ni(Pr^ixa)_2$-(pyz) (Pr^ixa = propylxanthate = i-$C_3H_7OCS_2^-$) is comparatively large even though its Ni(II) center is substantially more distorted than that of **1**.[85]

In addition, **1** and **2** exhibit markedly different pyz tilt angles, with **2** being intermediate (72.8°) between the two unique angles found in **1** (53.1 and 88.5°). For the $[Cu(HF_2)(pyz)_2]X$ series, there is an apparent correlation between the pyz tilt angles such that octahedral X^- gave larger $J_\perp$ values than when X^- was a tetrahedral anion. Representative examples are X = BF_4^- and SbF_6^- as their tilt angles are 59.4 and 81.4°, respectively; thus the greater $J_\perp$ seems to occur when the pyz tilt angle achieves near perpendicularity to the CuN_4 plane.[7,10] A similar trend may occur in the Ni(II) systems although the differences in local coordination symmetry can greatly influence the superexchange as well. If the Ni-pyz-Ni magnetic interaction was strictly governed by the σ-bond network then the pyz tilt angle would be inconsequential (a priori). Then, it seems that the spin exchange strength would depend more on the Ni−N/Ni−F bond distances and relative trajectory (or disposition) along the Ni−N···N−Ni and Ni−F···F−Ni directions; these torsion angles are 179.7, 180, and 170° for **1** and rigorously 180, 180 and 180° for **2**. As suggested from Table 5, perhaps a more sensitive measure of the distortion along the two types of spin exchange paths is the consideration of a simple three-atom segment, namely, Ni−N···N and Ni−F···F.

The average pyz tilt angle of **1** is 70.8°, which is very similar to that of **2**. However, the model employed above assumed that the two unique Ni-pyz-Ni pathways gave the same exchange constant which may be an oversimplification. Because of the differing values of *S* for Cu(II) and Ni(II) we cannot directly compare their $J_\perp$ values (i.e., Ni-pyz-Ni) but we can compare the net effective exchange integral $4S^2J$ for the various compounds including $[M(HF_2)(pyz)_2]X$ (M = Ni, Cu; X = PF_6^-, SbF_6^-).[7,10] From Table 6 it can be seen that **1**, **2**, and $Ni(Pr^ixa)_2(pyz)$[85] exhibit relatively large J and $4S^2J$ values while the other compounds are significantly lower. More definitive comparisons cannot be made because of the lack of structural and magnetic data for many of the listed Ni(II) compounds. Table 7 lists selected Cu(II)-pyrazine coordination polymers along with various magnetostructural parameters.[6,7,10,18,19,88,89] Collectively, the Cu(II) systems show larger exchange integrals as compared to the Ni(II) materials most probably because the magnetic orbital of a Cu(II) ion has a stronger contribution from its first-coordinate ligand atoms than the magnetic orbitals of a Ni(II) ion.

Another important factor worthy of consideration is the probable dependency on *M*-N bond lengths (where Cu−N is ~0.1−0.2 Å shorter than Ni−N) as well as the extent of spin delocalization from the Cu(II) ion onto the bridging pyz ligand. The same argument should be applicable to Ni(II). From analysis of ^{13}C NMR frequency shifts in 1D $Cu(NO_3)_2(pyz)$, it was recently determined that 10% of the spin moment is transferred from the Cu(II) ion to the coordinated nitrogen atom of the pyz ring.[90] A related study on $Cu(NO_3)_2(H_2O)_2(pym)$ (pym = pyrimidine) revealed very similar results.[91]

Table 6. Comparison of Key Structural Parameters, J Constants, and Exchange Integrals for Several Antiferromagnetic Ni(II)-Pyrazine Coordination Polymers. ($J > 0$ Refers to Antiferromagnetic Coupling)[a]

compound	z	Ni−N (Å)	Ni−X (Å)	Pyz tilt angle (deg)	J (K)[c]	$4S^2J$	reference
$[Ni(pyz)(H_2O)_4](NO_3)_2$	2	2.112	2.039[b]	51.6	N/A	N/A	83
$[Ni(2\text{-}mpac)_2(pyz)]\cdot 4H_2O$	2	2.100[b]	2.042[b]	66.9	N/A	N/A	84
$Ni(Pr^{i}xa)_2(pyz)$	2	2.150	2.418	N/A	2.67	10.7	85
$NiCl_2(pyz)_2$	4?	N/A	N/A	N/A	0.55	2.2	86
$NiBr_2(pyz)_2$	4	2.154	2.570	47.5	0.12	0.48	47
$Ni(NCO)_2(pyz)_2$	4	2.139	2.021	52.7	0.69	2.8	48
$Ni(NCS)_2(pyz)_2$	4	2.272[b]	1.945	44.3	N/A	N/A	49
$Ni(NO_3)_2(pyz)_2$	4?	N/A	N/A	N/A	0.13	0.52	87
$[Ni(HF_2)(pyz)_2]PF_6$ (**1**)	4	2.151	2.025	88.5, 53.1	2.5	10.0	this work
$[Ni(HF_2)(pyz)_2]SbF_6$ (**2**)	4	2.123	2.099	72.8	9.2	36.8	this work

[a] N/A = unreported value. 2-mpac = 5-methyl-2-pyrazinecarboxylic acid. $Pr^{i}xa$ = propylxanthate ion = $i\text{-}C_3H_7OCS_2^-$. For **1** and **2**, the italicized J-values refer to computationally determined $J_\perp$'s as described in the text and are likely overestimated by a factor of up to 4. z = number of pyz ligands coordinated to an octahedral Ni(II) center. [b] Refers to an average bond length. [c] Corresponds to the Ni-pyz-Ni magnetic interaction when other exchange pathways coexist.

Table 7. Structural and Magnetic Properties of Selected Antiferromagnetic Cu(II)-Pyrazine Coordination Polymers ($J > 0$ Indicates an Antiferromagnetic Interaction)

compound	z[b]	Cu−N (Å)	Cu−X (Å)	Pyz tilt angle (deg)	J (K)[c,d]	reference
$Cu(NO_3)_2(pyz)$	2	1.984	2.010, 2.490	51.0	10.8	88
$Cu(hfac)_2(pyz)$	2	2.529	1.924, 2.004	N/A[e]	∼0	89
$Cu(BF_4)_2(pyz)_2$[a]	4	2.042	2.338	67.4	15.3	18
$Cu(ClO_4)_2(pyz)_2$	4	2.051	2.361	65.8	17.5	18
$[Cu(NO_3)(pyz)_2]PF_6$[a]	4	2.042	2.413	61.4	10.8	18
$[Cu(NO_2)(pyz)_2]ClO_4$	4	2.049	2.285	59.7	8.9	19
$[Cu(HF_2)(pyz)_2]BF_4$	4	2.040	2.207	59.4	5.7	7
$[Cu(HF_2)(pyz)_2]PF_6$	4	2.040	2.311	79.9	12.8	9
$[Cu(HF_2)(pyz)_2]SbF_6$	4	2.049	2.338	81.4	13.4	10

[a] X-ray structure determined at 160 K. [b] Number of pyz ligands coordinated to the octahedral Cu(II) ion. [c] Corresponds to the Cu-pyz-Cu magnetic interaction if other exchange pathways coexist. [d] For $S = 1/2$, J is identical to the exchange integral. [e] The nitrogen lone-pair orbitals on the pyrazine ligand interact with the spin-paired Cu d_{z^2} orbital. N/A = unreported value.

A spin polarization mechanism can be invoked to describe the ability of an unpaired electron on one atom (Ni in the case of **1** and **2**) to polarize the electron cloud on adjacent atoms in the opposite sense.[50] This will yield an alternation of the spin density of each atom contained in the polyatomic bridge. Since the $d_{x^2-y^2}$ and d_{z^2} orbitals of the Ni(II) ion each contain one unpaired electron, the pyz and HF_2^- bridging units will carry some spin density. Regardless of the identity and oxidation state of M, M-pyz-M magnetic interactions are always antiferromagnetic, that is, M(↑)-N(↓)-C(↑)-C(↓)-N(↑)-M(↓); however, the strength of these interactions vary considerably.

Let us now consider the sign of the magnetic interaction along Ni-FHF-Ni. While this interaction is stronger than Ni-pyz-Ni, magnetic susceptibility data and DFT calculations suggest that it must support antiferromagnetic coupling. This can be rationalized by the simple spin polarization scheme,[50] Ni(↑)-F(↓)-H-F(↑)-Ni(↓), which precludes significant spin density on the central H despite its important placement in the superexchange path. Should spin density reside on the hydrogen atom, a ferromagnetic interaction between Ni(II) ions may be anticipated in accord with Ni(↑)-F(↓)-H(↑)-F(↓)-Ni(↑). It stands to reason that the more electron-withdrawing ability of the HF_2^- ligand (relative to pyz) should generate more spin density along this bridge if we consider only the σ-type orbitals involved in the spin exchange. As the spin density is siphoned toward/away from a ligand, its contribution to the electronic coupling will be enhanced/diminished. These behaviors are manifested experimentally by the exchange anisotropy in **1** and **2** where we showed that the Ni-FHF-Ni interaction is stronger than Ni-pyz-Ni.

5. CONCLUDING REMARKS

Two new Ni(II)-bifluoride coordination polymers are reported along with their structural, electronic, and magnetic properties. $[Ni(HF_2)(pyz)_2]PF_6$ (**1**) and $[Ni(HF_2)(pyz)_2]SbF_6$ (**2**) feature 3D pseudocubic frameworks composed of 1D Ni-FHF-Ni chains (along the c-axis) that are connected via μ-pyz ligands in the ab-plane. Taken together, magnetic property measurements combined with theoretical insights reveal significant exchange couplings along the Ni-FHF-Ni pathways (J_{1D}), which is stronger in **2** relative to **1** owing to bent Ni-FHF-Ni linkages in the latter which are linear in **2**. The exchange interaction along Ni-pyz-Ni ($J_\perp$) is also stronger in **2** than in **1** because the Ni−N···N backbone is rigorously linear in **2** but distorted in **1** because of the lower crystal symmetry. Several different models can be used to interpret magnetic susceptibility data obtained for powder samples of **1** and **2** above the broad maximum. Fits to these models are compatible with the results of DFT calculations which predict that $J_{1D} > J_{\perp}$. Ligand field analysis of room temperature electronic absorption spectra suggests that $D < 0$ for **1** and $D > 0$ for **2** despite their common NiN_4F_2 cores. The most sensible D parameters found from the LFT analysis are -5.2 cm^{-1} and 7.8 cm^{-1} for **1** and **2**, respectively, which, should they remain invariant with temperature, are likely to be too large to stabilize the Haldane phase. This is in keeping with the results of pulsed-field magnetization and μSR data, which show no evidence for a spin gap. To be more definitive about the contributions of $J_{\perp}$ (and D) to the magnetic behavior of **1** and **2**, suitable single crystals are required for detailed studies. Also, the contrasting low temperature structural modifications exhibited by the NiN_4F_2 cores of **1** and **2** require complementary spectroscopic data to re-evaluate the ligand-field and D parameters. Coordination polymers containing only Ni-FHF-Ni linkages are being developed to further examine the range and sign of these interactions.

■ ASSOCIATED CONTENT

Ⓢ **Supporting Information.** X-ray crystallographic details in CIF format, χT vs T and $1/\chi$ vs T plots as well as figures illustrating the total spin exchange energies for the possible spin states of **1** and **2**. This material is available free of charge via the Internet at http://pubs.acs.org.

■ AUTHOR INFORMATION

Corresponding Authors

*Phone: (509) 359-2878 (J.L.M), (631) 632-8156 (P.W.S.). Fax: (509) 359-6973 (J.L.M), (631) 632-8176 (P.W.S.). E-mail: jmanson@ewu.edu (J.L.M), pstephens@stonybrook.edu (P.W.S.).

■ ACKNOWLEDGMENT

Work at EWU was supported by the National Science Foundation (NSF) under Grant DMR-1005825. Research performed at North Carolina State University was supported by the Office of Basic Energy Sciences (BES), Division of Materials Sciences of the U.S. Department of Energy (DoE) under Grant DE-FG02-86ER45259 and by the computing resources of the NERSC and HPC Centers. A portion of this work was performed at the National High Magnetic Field Laboratory, which is supported by the NSF Cooperative Agreement No. DMR-0654118, the State of Florida, and the U.S. DoE BES program "Science in 100 T." Research carried out in part at the National Synchrotron Light Source (NSLS) at Brookhaven National Laboratory, was supported by the U.S. DoE, Office of Science, BES, under Contract No. DE-AC02-98CH10886. The work done by S. Zvyagin was partially supported by the Deutsche Forschungsgemeinschaft and EuroMagNET (under contract No. 228043). This work was also supported by the EPSRC, U.K. Some of this work made use of the Swiss Muon Source, Paul Scherrer Institut, Switzerland. We are grateful to A. Amato (PSI) and M. Ozerov (HLD) for technical assistance.

■ REFERENCES

(1) For example, see: Bhattacharyya, K. *Acc. Chem. Res.* **2003**, *36*, 95.

(2) Goeltz, J. C.; Kubiak, C. P. *J. Am. Chem. Soc.* **2010**, *132*, 17390.

(3) Jeffrey, G. A. *An Introduction to Hydrogen Bonding*, Oxford Univ. Press: New York, 1997.

(4) Desiraju, G.; Steiner, T. *The Weak Hydrogen Bond in Structural Chemistry and Biology*; Oxford Univ. Press: New York, 2001.

(5) (a) Emsley, J. *Chem. Soc. Rev.* **1980**, *9*, 91. (b) Janssen, C. L.; Allen, W. D.; Schaefer, H. F. *Chem. Phys. Lett.* **1986**, *131*, 352.

(6) Manson, J. L.; Conner, M. M.; Schlueter, J. A.; McConnell, A. C.; Southerland, H. I.; Malfant, I.; Lancaster, T.; Blundell, S. J.; Brooks, M. L.; Pratt, F. L.; Singleton, J.; McDonald, R. D.; Lee, C.; Whangbo, M.-H. *Chem. Mater.* **2008**, *20*, 7408.

(7) Manson, J. L.; Conner, M. M.; Schlueter, J. A.; Lancaster, T.; Blundell, S. J.; Brooks, M. L.; Pratt, F. L.; Papageorgiou, T.; Bianchi, A. D.; Wosnitza, J.; Whangbo, M.-H. *Chem. Commun.* **2006**, 4894.

(8) Sengupta, S.; Batista, C. D.; McDonald, R. D.; Cox, S.; Singleton, J.; Huang, L.; Papageorgiou, T. P.; Ignatchik, O.; Herrmannsdorfer, T.; Manson, J. L.; Schlueter, J. A.; Funk, K. A.; Wosnitza, J. *Phys. Rev. B* **2009**, *79*, 060409R.

(9) Cizmar, E.; Zvyagin, S. A.; Beyer, R.; Uhlarz, M.; Ozerov, M.; Skourski, Y.; Manson, J. L.; Schlueter, J. A.; Wosnitza, J. *Phys. Rev. B* **2010**, *81*, 064422.

(10) Manson, J. L.; Schlueter, J. A.; Funk, K. A.; Southerland, H. I.; Twamley, B.; Lancaster, T.; Blundell, S. J.; Baker, P. J.; Pratt, F. L.; Singleton, J.; McDonald, R. D.; Goddard, P. A.; Sengupta, P.; Batista, C. D.; Ding, L.; Lee, C.; Whangbo, M.-H.; Franke, I.; Cox, S.; Baines, C.; Trial, D. *J. Am. Chem. Soc.* **2009**, *131*, 6733.

(11) Emsley, J.; Parker, R. J.; Overill, R. E. *J. Chem. Soc., Faraday Trans. 2* **1982**, *79*, 1347.

(12) Pendas, A. M.; Blanco, M. A.; Francisco, E. *J. Chem. Phys.* **2006**, *125*, 184112.

(13) Clark, J. H.; Emsley, J.; Jones, D. J.; Overill, R. E. *J. Chem. Soc., Dalton Trans.* **1981**, 1219.

(14) Fujiwara, F. Y.; Martin, J. S. *J. Am. Chem. Soc.* **1974**, *96*, 7625.

(15) Keil, F.; Ahlrichs, R. *J. Am. Chem. Soc.* **1976**, *98*, 4787.

(16) Larson, J. W.; McMahon, T. B. *J. Am. Chem. Soc.* **1982**, *104*, 5848.

(17) *Handbook of Chemistry and Physics*, 91st ed.; CRC Press: New York, 2010−2011.

(18) Woodward, F. M.; Gibson, P. J.; Jameson, G. B.; Landee, C. P.; Turnbull, M. M.; Willett, R. D. *Inorg. Chem.* **2007**, *46*, 4256.

(19) Liu, T.; Chen, Y.-H.; Zhang, Y.-J.; Wang, Z.-M.; Gao, S. *Inorg. Chem.* **2006**, *45*, 9148.

(20) Richardson, H. W.; Wasson, J. R.; Hatfield, W. E. *Inorg. Chem.* **1977**, *16*, 484.

(21) Mohri, F.; Yoshizawa, K.; Yamabe, T.; Ishida, T.; Nogami, T. *Mol. Eng.* **1999**, *8*, 357.

(22) Belford, R. C. E.; Fenton, D. E.; Truter, M. R. *J. Chem. Soc., Dalton Trans.* **1972**, 2208.

(23) (a) *TOPAS V3: General profile and structure analysis software for powder diffraction data User's Manual*; Bruker AXS: Karlsruhe, Germany, 2005. (b) Coelho, A. A. *J. Appl. Crystallogr.* **2000**, *33*, 899.(c) *TOPAS-Academic* is available at www.topas-academic.net.

(24) Palatinus, L.; Chapuis, G. *J. Appl. Crystallogr.* **2007**, *40*, 786.

(25) Blundell, S. J. *Contemp. Phys.* **1999**, *40*, 175.

(26) Bachmann, R.; DiSalvo, F. J.; Geballe, T. H.; Greene, R. L.; Howard, R. E.; King, C. N.; Kirsch, H. C.; Lee, K. N.; Schwall, R. E.; Thomas, H.-U.; Zubeck, R. B. *Rev. Sci. Instrum.* **1972**, *43*, 205.

(27) Riegel, S.; Weber, G. *J. Phys. E: Sci. Instrum.* **1986**, *19*, 790.

(28) Zvyagin, S. A.; Krzystek, J.; van Loosdrecht, P. H. M.; Dhalenne, G.; Revcolevschi, A. *Phys. B* **2004**, *1*, 346.

(29) (a) Kresse, G.; Hafner, J. *Phys. Rev. B* **1993**, *47*, 558. (b) Kresse, G.; Furthmüller, J. *Comput. Mater. Sci.* **1996**, *6*, 15. (c) Kresse, G.; Furthmüller, J. *Phys. Rev. B* **1996**, *54*, 11169.

(30) Perdew, J. P.; Burke, K.; Ernzerhof, M. *Phys. Rev. Lett.* **1996**, *77*, 3865.

(31) Dudarev, S. L.; Botton, G. A.; Savrasov, S. Y.; Humphreys, C. J.; Sutton, A. P. *Phys. Rev. B* **1998**, *57*, 1505.

(32) Bendix, J. *Compr. Coord. Chem. II* **2004**, *2*, 673.

(33) Innes, K. K.; Byrne, J. P.; Ross, I. G. *J. Mol. Spectrosc.* **1967**, *22*, 125.

(34) Nakamoto, K. *Infrared and Raman Spectra of Inorganic and Coordination Compounds*, 5th ed.; John Wiley and Sons: New York, 1997.

(35) (a) Glerup, J.; Mønsted, O.; Schäffer, C. E. *Inorg. Chem.* **1976**, *15*, 1399. (b) Dubicki, L.; Hitchmann, M. A.; Day, P. *Inorg. Chem.* **1970**, *9*, 188. (c) Dubicki, L.; Day, P. *Inorg. Chem.* **1971**, *10*, 2043.

(36) Lever, A. B. P. *Inorganic Electronic Spectroscopy*; Elsevier: New York, 1984.

(37) Hare, C. R.; Ballhausen, C. J. *J. Chem. Phys.* **1964**, *40*, 792.

(38) (a) Kennedy, B. J.; Murray, K. S.; Hitchman, M. A.; Rowbottom, G. L. *J. Chem. Soc., Dalton Trans.* **1987**, 825. (b) Merriam, J. S.; Perumareddi, J. R. *J. Phys. Chem.* **1975**, *79*, 142. (c) Goldstein, M.; Taylor, F. B.; Unsworth, W. D. *J. Chem. Soc., Dalton Trans.* **1972**, 418. (d) Ribbing, C.; Odelius, M.; Kowalewski, J. *Mol. Phys.* **1991**, *74*, 1299.

(39) (a) Vermaas, A.; Groeneveld, W. L.; Reedijk, J. *Z. Naturforsch.* **1977**, *32a*, 632. (b) Reimann, C. W. *J. Phys. Chem.* **1970**, *74*, 561.

(40) Driessen, R. A. J.; Hulsbergen, F. B.; Vermin, W. J.; Reedijk, J. *Inorg. Chem.* **1982**, *21*, 3594.

(41) (a) Ferguson, J.; Guggenheim, H. J.; Wood, D. L. *J. Chem. Phys.* **1964**, *40*, 822. (b) Shulman, R. G.; Knox, K. *Phys. Rev. Lett.* **1960**, *4*, 603. (c) Sugano, S.; Shulman, R. G. *Phys. Rev.* **1963**, *130*, 517.

(42) (a) Schäffer, C. E. *Struct. Bonding (Berlin)* **1968**, *5*, 68. (b) Schäffer, C. E.; Jørgensen, C. K. *Mol. Phys.* **1965**, *9*, 401. (c) Yamatera, H. *Bull. Chem. Soc. Jpn.* **1958**, *31*, 95.

(43) Bendix, J.; Brorson, M.; Schäffer, C. E. *Inorg. Chem.* **1993**, *32*, 2838.

(44) Bendix, J.; Bøgevig, A. *Inorg. Chem.* **1998**, *37*, 5992.

(45) Bendix, J.; Brorson, M.; Schäffer, C. E. *Coord. Chem. Rev.* **1989**, *94*, 181.

(46) (a) Balz, D.; Pleith, K. *Z. Elektrochem.* **1955**, *59*, 545. (b) Birgeneau, R. J.; Guggenheim, H. J.; Shirane, G. *Phys. Rev. B* **1970**, *1*, 2211.

(47) James, M. *Aust. J. Chem.* **2002**, *55*, 219.

(48) Wang, Q.-L.; Qi, F.; Yang, G.; Liao, D.-Z.; Yang, G.-M.; Ren, H.-X. *Z. Anorg. Allg. Chem.* **2010**, *636*, 634.

(49) Wriedt, M.; Je*β*, I.; Näther, C. *Eur. J. Inorg. Chem.* **2009**, 1406.

(50) Kahn, O. *Molecular Magnetism*; VCH Publishers: Weinheim, 1993.

(51) Birgeneau, R. J.; DeRosa, F.; Guggenheim, H. J. *Solid State Commun.* **1970**, *8*, 13.

(52) Rushbrooke, G. S.; Wood, P. *J. Mol. Phys.* **1963**, *6*, 409.

(53) Lines, M. E. *Phys. Rev.* **1967**, *164*, 736.

(54) Okazaki, A.; Suemune, Y. *J. Phys. Soc. Jpn.* **1961**, *16*, 671.

(55) (a) Sykes, M. F.; Fisher, M. E. *Phil. Mag.* **1962**, *7*, 1731. (b) Fisher, M. E. *Physica* **1962**, *28*, 919.

(56) Goddard, P. A.; Singleton, J.; Sengupta, P.; McDonald, R. D.; Lancaster, T.; Blundell, S. J.; Pratt, F. L.; Cox, S.; Harrison, N.; Manson, J. L.; Southerland, H. I.; Schlueter, J. A. *New J. Phys.* **2008**, *10*, 083025.

(57) Miedema, A. R.; de Jongh, L. J. *Adv. Phys.* **1974**, *23*, 1.

(58) (a) Manson, J. L.; Lancaster, T.; Blundell, S. J.; Qiu, Y.; Singleton, J.; Sengupta, P.; Pratt, F. L.; Kang, J.; Lee, C.; Whangbo, M.-H. *Polyhedron* **2010**, *29*, 514. (b) Manson, J. L.; Stone, K. H.; Southerland, H. I.; Lancaster, T.; Steele, A. J.; Blundell, S. J.; Pratt, F. L.; Baker, P. J.; McDonald, R. D.; Sengupta, P.; Singleton, J.; Goddard, P. A.; Lee, C.; Whangbo, M.-H.; Warter, M. L.; Mielke, C. H.; Stephens, P. W. *J. Am. Chem. Soc.* **2009**, *131*, 4590. (c) Lancaster, T.; Blundell, S. J.; Baker, P. J.; Brooks, M. L.; Hayes, W.; Pratt, F. L.; Manson, J. L.; Conner, M. M.; Schlueter, J. A. *Phys. Rev. Lett.* **2007**, *99*, 267601. (d) Lancaster, T.; Blundell, S. J.; Brooks, M. L.; Baker, P. J.; Pratt, F. L.; Manson, J. L.; Conner, M. M.; Xiao, F.; Landee, C. P.; Chaves, F. A.; Soriano, S.; Novak, M. A.; Papageorgiou, T.; Bianchi, A. D.; Herrmannsdörfer, T.; Wosnitza, J.; Schlueter, J. A. *Phys. Rev. B* **2007**, *75*, 094421. (e) Manson, J. L.; Lancaster, T.; Schlueter, J. A.; Blundell, S. J.; Brooks, M. L.; Pratt, F. L.; Nygren, C. L.; Koo, H.-J.; Dai, D.; Whangbo, M.-H. *Inorg. Chem.* **2007**, *46*, 213. (f) Lancaster, T.; Blundell, S. J.; Brooks, M. L.; Baker, P. J.; Pratt, F. L.; Manson, J. L.; Landee, C. P.; Baines, C. *Phys. Rev. B* **2006**, *73*, 020410R. (g) Lancaster, T.; Blundell, S. J.; Brooks, M. L.; Baker, P. J.; Pratt, F. L.; Manson, J. L.; Baines, C. *Phys. Rev. B* **2006**, *73*, 172403. (h) Manson, J. L.; Lancaster, T.; Chapon, L. C.; Blundell, S. J.; Schlueter, J. A.; Brooks, M. L.; Pratt, F. L.; Nygren, C. L.; Qualls, J. S. *Inorg. Chem.* **2005**, *44*, 989. (i) Lancaster, T.; Blundell, S. J.; Pratt, F. L.; Brooks, M. L.; Manson, J. L.; Brechin, E. K.; Cadiou, C.; Low, D.; McInnes, E. J. L.; Winpenny, R. E. P. *J. Phys.: Condens. Matter* **2004**, *16*, S4563.

(59) Hayano, R. S.; Uemura, Y. J.; Imazato, J.; Nishida, N.; Yamazaki, T.; Kubo, R. *Phys. Rev. B* **1979**, *20*, 850.

(60) Blundell, S. J. *Magnetism in Condensed Matter*; Oxford University Press: Oxford, 2001.

(61) Sorai, M.; Nakano, M.; Miyazaki, Y. *Chem. Rev.* **2006**, *106*, 976, and references therein.

(62) Weng, C. Y. Ph.D. Thesis, Carnegie-Mellon University, Pittsburgh, Pennsylvania, 1969.

(63) Meyer, A.; Gleizes, A.; Girerd, J. J.; Verdaguer, M.; Kahn, O. *Inorg. Chem.* **1982**, *21*, 1729.

(64) Smith, J.; Gerstein, B. C.; Liu, S. H.; Stucky, G. *J. Chem. Phys.* **1970**, *53*, 418.

(65) (a) Yamamoto, S.; Miyashita, S. *Phys. Rev. B* **1993**, *48*, 9528. (b) Yamamoto, S.; Miyashita, S. *Phys. Rev. B* **1994**, *50*, 6277.

(66) Becke, A. D. *Phys. Rev. A* **1988**, *38*, 3098.

(67) Lee, C.; Yang, W.; Parr, R. G. *Phys. Rev. B* **1988**, *37*, 785.

(68) Kim, K.; Jordan, K. D. *J. Phys. Chem.* **1994**, *98*, 10089.

(69) Frish, M. J. et al. *Gaussian 03*, B.04; Gaussian, Inc.: Pittsburgh, PA, 2003.

(70) Whangbo, M.-H.; Koo, H.-K.; Dai, D. *J. Solid State Chem.* **2003**, *176*, 417.

(71) (a) Xiang, H. J.; Lee, C.; Whangbo, M.-H. *Phys. Rev. B.* **2007**, *76*, 220411(R). (b) Koo, H.-J.; Whangbo, M.-H. *Inorg. Chem.* **2008**, *47*, 128. (c) Koo, H.-J.; Whangbo, M.-H. *Inorg. Chem.* **2008**, *47*, 4779.

(72) Achiwa, N. *J. Phys. Soc. Jpn.* **1969**, *27*, 561.

(73) Mekata, M.; Adachi, K.; Takadi, H.; Achiwa, N. In *Proceedings of the 12th International Conference on Low Temperature Physics*, Kyoto Japan, 1970; Keigaku Publishing Co.: Tokyo, Japan, 1970.

(74) Davidson, E. *Int. J. Quantum Chem.* **2004**, *98*, 317.

(75) Figgis, B. N. *Introduction to Ligand Fields*; Interscience Publishers: New York, 1966.

(76) Titiš, J.; Boča, R. *Inorg. Chem.* **2010**, *49*, 3971, and references therein.

(77) Rogez, G.; Rebilly, J.-N.; Barra, A.-L.; Sorace, L.; Blondin, G.; Kirchner, N.; Duran, M.; van Slageren, J.; Parsons, S.; Ricard, L.; Marvilliers, A.; Mallah, T. *Angew. Chem., Int. Ed.* **2005**, *44*, 1876.

(78) Boča, R.; Baran, P.; Diháò, L.; Hvastijová, M.; Witschek, G. *Chem. Phys. Lett.* **1998**, *284*, 254.

(79) Dobrzynska, D.; Jerzykiewicz, L. B.; Duczmal, M.; Wojciechowska, A.; Jablonska, K.; Palus, J.; Ozarowski, A. *Inorg. Chem.* **2006**, *45*, 10479.

(80) Abragam, A.; Bleaney, B. *Electron Paramagnetic Resonance of Transition Ions*; Clarendon: Oxford, 1970.

(81) Turov, E. A. *Physical Properties of Magnetically Ordered Crystals*; Academic Press: New York, 1965.

(82) (a) Krzystek, J.; Zvyagin, S. A.; Ozarowski, A.; Trofimenko, A.; Telser, J. *J. Magn. Reson.* **2006**, *178*, 174. (b) Krzystek, J.; Ozarowski, A.; Telser, J. *Coord. Chem. Rev.* **2006**, *250*, 2308.

(83) Choudhury, C. R.; Dey, S. K.; Sen, S.; Bag, B.; Mitra, S.; Gramlich, V. *Z. Naturforsch.* **2002**, *57b*, 1191.

(84) Chen, S.-P.; Fan, G.; Gao, S.-H. *Z. Anorg. Allg. Chem.* **2008**, *634*, 539.

(85) (a) Trávniček, Z.; Pastorek, R.; Šindelař, Z.; Kameniček, J. *Polyhedron* **1996**, *15*, 2975. (b) Orendáčová, A.; Zorkovská, A.; Park, J.-H.; Orendáč, M.; Trávniček, Z.; Feher, A.; Meisel, M. W. *Phys. Status Solidi C* **2006**, *3*, 134.

(86) Goldstein, M.; Taylor, F. B.; Unsworth, W. D. *J. Chem. Soc., Dalton Trans.* **1972**, 418.

(87) Otieno, T.; Thompson, R. C. *Can. J. Chem.* **1995**, *73*, 275.

(88) (a) Hammar, P. R.; Stone, M. B.; Reich, D. H.; Broholm, C.; Gibson, P. J.; Turnbull, M. M.; Landee, C. P.; Oshikawa, M. *Phys. Rev. B* **1999**, *59*, 1008. (b) Losee, D. B.; Richardson, H. W.; Hatfield, W. E. *J. Chem. Phys.* **1973**, *59*, 3600.

(89) Belford, R. C. E.; Fenton, D. E.; Truter, M. R. *J. Chem. Soc., Dalton Trans.* **1974**, 17.

(90) Kühne, H.; Günther, M.; Grossjohann, S.; Brenig, W.; Litterst, F. J.; Reyes, A. P.; Kuhns, P. L.; Turnbull, M. M.; Landee, C. P.; Klauss, H.-H. *Phys. Status Solidi B* **2010**, *247*, 671.

(91) Wolter, A. U. B.; Wzietek, P.; Süllow, S.; Litterst, F. J.; Honecker, A.; Brenig, W.; Feyerherm., R.; Klauss, H.-H. *Phys. Rev. Lett.* **2005**, *94*, 057204.